Journal of Southeast University (English Edition)　Vol. 42, No. 1, pp. 36-54　Mar. 2026　ISSN 1003-7985

Experimental investigation of the flow-structure interaction mechanism of flutter for an 8∶1 rectangular flat plate

LI Wenjie, LAIMA Shujin

(1. Key Laboratory of Structures Dynamic Behavior and Control of Ministry of Education, Harbin Institute of Technology, Harbin 150090, China; 2. Key Laboratory of Smart Prevention and Mitigation of Civil Engineering Disasters of Ministry of Industry and Information Technology, Harbin Institute of Technology, Harbin 150090, China; 3. School of Civil Engineering, Harbin Institute of Technology, Harbin 150090, China)

Abstract: The intrinsic interaction mechanism of flutter between the flow and structure of a rectangular plate remains a mystery from the viewpoint of unsteady flow. The present study provides a novel insight into this interaction mechanism based on an adequate understanding of the formation and evolution of the flapping leading-edge vortex (LEV). A series of wind tunnel tests was conducted to investigate the nonlinear flutter instability of an 8∶1 rectangular plate. The complete flow fields around the model throughout the flutter process were obtained by a particle image velocimetry (PIV) technique using two synchronous cameras with an interpolation and resampling method. To acquire the flow structures corresponding to the characteristic frequency of flutter, the spectral proper orthogonal decomposition (SPOD) method was extended to a noninertial frame to reconstruct the low-rank flow field during flutter and extract the characteristic flow pattern coupled with oscillations. It was found that when the 8∶1 rectangular plate undergoes flutter, the LEVs exhibit a periodic flapping phenomenon induced by the structure oscillations. A two-dimensional correlation analysis of the flapping LEVs was conducted for different inflow velocities. The results demonstrate that there is a substantial phase lead phenomenon in the LEV evolution downstream for a higher inflow velocity. This phenomenon may be related to a phase offset of aerodynamic forces, and finally, it gives rise to flutter.

Key words: flutter; aerodynamic instability; fluid-structure interaction; leading-edge vortex (LEV); spectral proper orthogonal decomposition (SPOD)

DOI: 10. 3969/j. issn. 1003-7985. 2026. 01. 004

Understanding and improving the flutter stability of long-span suspension bridges is a recurring and vital theme in bridge engineering. In the past decades, the flutter of long-span suspension bridges—as a representative phenomenon of aeroelastic instability—has been studied extensively and understood well from the viewpoint of structural dynamics. A classical and fundamental theory proposed by Scanlan et al. [1], known as the flutter derivative theory, considered the aerodynamic self-excited forces as a series of linearized functions of the motion states, i. e., displacements and velocities, and the corresponding coefficients were termed as flutter derivatives. In Scanlan aerodynamic model, the flutter derivative A_2^* of the angular velocity term is regarded as the main controlling factor of the single-degree-of-freedom torsional flutter based on a linear stability analysis—which is related to the concept of the aerodynamic damping[2]. Considerable research efforts have been directed to improving Scanlan theory in higher dimensions, and good performance has been achieved in predicting the flutter critical wind speed[3-8].

A strong nonlinearity has been widely observed in the dynamic behaviors of flutter for certain bluff aerodynamic shapes or at large angles of attack, attracting considerable attention from many researchers in recent years[9-16]. A limit cycle oscillation (LCO) with a stable amplitude can be induced when the inflow velocity exceeds the flutter critical wind speed—this LCO forms a striking contrast, with a rapid diversity of the bending-torsional coupling flutter. The classical linear theory cannot describe nonlinear flutter behaviors. Much research has focused on exploring and modeling the aerodynamic characteristics of nonlinear flutter. Scanlan[17] and Noda et al. [18] pointed out that the flutter derivatives are affected by the oscillation amplitude for a rectangular section with a large aspect ratio. A series of nonlinear aerodynamic models was proposed to construct a nonlinear mapping from motion states to self-excited forces; these models were used to predict the dynamic responses of nonlinear flutter accurately. Such modeling methods can be classified roughly into three categories: high-order polynomials[12, 19-22], modified nonlinear flutter derivatives[23-25], and neural networks[26-28]. The first two ap-

---

Received 2025-05-07, **Revised** 2025-09-06.

Biographies: LI Wenjie (1994—), male, doctor; LAIMA Shujin (corresponding author), male, doctor, professor, laimashujin@hit. edu. cn.

Foundation items: The National Natural Science Foundation of China (No. 52178470), the National Key Research and Development Program of China (No. 2022YFC3005303).

Citation: LI Wenjie, LAIMA Shujin. Experimental investigation of the flow-structure interaction mechanism of flutter for an 8∶1 rectangular flat plate[J]. Journal of Southeast University (English Edition), 2026, 42(1): 36-54. DOI: 10. 3969/j. issn. 1003-7985. 2026. 01. 004.

proaches are identical in essence, and research into these approaches indicated that the structural dynamic mechanism of nonlinear flutter could be attributed to the amplitude-dependent nonlinearity of negative aerodynamic damping. However, compared with the advances in understanding the structural dynamic mechanism, there is still a long way to go to fully comprehend the intrinsic interaction mechanism of flutter from the viewpoint of unsteady flows. A comprehensive investigation of the unsteady flow around the structure during flutter is necessary to clarify the flow-structure interaction process.

An interesting and important characteristic of unsteady flow around a bluff body is the vortical structure near the leading edge. Matsumoto et al. [29] and Bhat et al. [30] remarked that the flow separation at the leading edge plays an important role in the flutter behaviors. However, the specific flow evolution process related to flutter onset remains unknown. Hu et al. [31-32] explored the vortex motion pattern around the bridge deck during vortex-induced vibrations based on a correlation analysis of surface pressure data. The formation and evolution of the leading-edge vortex (LEV) have been widely investigated in the field of airfoil dynamic stall and bio-inspired flight[33-37]. An attached LEV can significantly enhance the lift acting on the airfoil with a large angle of attack; subsequently, the lift drops rapidly as the LEV separates from the trailing edge[38]. Baik et al. [33] experimentally investigated the development of LEV trajectory and circulation for a pitching and plunging flat-plate aerofoil oscillating sinusoidally in the amplitude range of 6° to 22°. They reported that the LEV flow evolution is independent of the Strouhal number and is determined by the effective angle of attack and reduced frequency. Onoue and Breuer[35] reported the formation and evolution processes of the LEV for a pitching flat plate that is made to oscillate with a large amplitude of 93° by a forced vibration method using a cyber-physical system. Based on the measured vortex circulation and position, a potential flow model coupled with the steady moment of the plate was proposed. This model demonstrated robust performance in predicting the aerodynamic torque on the plate. Menon and Mittal[11] investigated the effect of spring stiffness, equilibrium angle-of-attack, and location of the elastic axis on the onset of torsional flutter at a Reynolds number of 1 000. They demonstrated that the critical state of the torsional flutter is determined by a specific time parameter related to a shear-layer instability, namely, the recovery time of the moment coefficient from a small perturbation on the angle of attack to the steady state. Li et al. [36] experimentally studied the formation and detachment mechanisms of the LEV for a pitching and plunging flat plate under different maximum effective angles of attack (12°-24°) and three flow topologies (quasisteady development, boundary-layer eruption, and secondary vortex formation). They found that the mechanisms depended on the leading-edge shear-layer angle. These results provide a prominent indication that the unsteady flow at the leading edge is closely related to the oscillation features of the structure. In contrast, the aerodynamic characteristics acting on the structure are also affected remarkably by the formation and evolution of the shear layer at the leading edge and consequent LEV. Therefore, a reasonable speculation can be deduced that the flow topology at the leading edge, such as the separated shear layer and LEV, can be a vital tie between the flow and structure and provide a potential trigger to the occurrence of flutter.

Matsumoto et al. [29] found that for rectangular plates, torsional flutter and coupled flutter typically are sensitive to a specific range of aspect ratios (B/H, B and H are the width and height of the model sections). Torsional flutter occurs at $B/H < 10$, while coupled flutter occurs at $B/H > 10$. However, Mills et al. [39] observed that for a stationary rectangular plate with B/H between 7.6 and 16, the flow pattern is quite similar at a high Re (i. e., $Re > 1\times10^4$): a separation bubble forms near the leading edge, and spanwise vortexes exhibit convection downstream due to the Kelvin-Helmholtz instability. Interestingly, even though the flow patterns around stationary plates are similar across B/H values, the type of flutter that occurs can be quite different. To better understand this discrepancy and gain deeper insight into the flutter mechanism for a bluff aerodynamic shape, a rectangular plate of B/H = 8∶1 was chosen in this study to examine the unsteady flow pattern coupled with oscillations. A series of wind tunnel tests was implemented to comprehensively investigate the unsteady flow characteristics around an 8∶1 rectangular flat plate before and after flutter. A spectral proper orthogonal decomposition (SPOD) method was applied to reconstruct a low-rank, high-fidelity flow field and extract the flapping vortex structure at the leading edge. This structure is related to the characteristic frequency induced by the model oscillation. The evolution processes of the flapping LEVs were compared, and a two-dimensional correlation analysis was conducted for different inflow velocities based on the SPOD-reconstructed vorticity distributions around the model. An intrinsic interaction mechanism of flutter was determined from the viewpoint of the flapping LEVs. This mechanism was attributed to the phase lead phenomenon during LEV evolution downstream for different inflow velocities.

1 Experimental Setup

1.1 Wind tunnel test

Flutter tests were conducted in a closed-circuit wind tunnel, SMC-WT1, at the Joint Laboratory of Wind Tunnel and Wave Flume, Harbin Institute of Technology, China. The test section of the wind tunnel with a cross section of 500 mm × 500 mm was 1 000 mm long. It was made of transparent acrylic plates, which allowed flow measurement by a particle image velocimetry (PIV) technique. The inflow wind velocity can be adjusted from 0 m/s to 25 m/s with a low turbulence intensity of less than 0.5%.

To excite LCOs of nonlinear flutter, a bluff section model, i. e., a rectangular flat plate with an aspect ratio of 8∶1, was mounted on a two-degree-of-freedom (vertical and torsional) spring-suspended test platform. The model dimensions were as follows: the width $B = 240$ mm, and the height $H = 30$ mm. Samples were manufactured by 3D printing using high-strength photosensitive resin with a density of 1.13 g/cm^3. The initial angle of attack of the model was set to 0°. The Reynolds number *Re* was calculated based on the model width. It approximately ranges from 4×10^4 to 2×10^5. Air bearings were used to completely restrict the inflow displacement of the model. Two laser displacement sensors (Keyence LK-G400) with a sample frequency of 1 kHz were installed symmetrically on both sides of the rotation axis to measure the vertical and torsional displacements of the rectangular flat plate. The measurement range of the laser displacement sensors is ±10 cm with a high resolution of 0.04 mm. This range is suitable for flutter response measurements with a large torsional amplitude of 15°. A detailed schematic diagram of the experimental setup is shown in Fig. 1, where α is the model torsional angle. To obtain the dynamic parameters of the model, a series of vertical and torsional free vibration tests was performed by imposing an initial large-amplitude excitation on the model at zero wind speed. All the structural dynamic parameters of the spring-suspended section model are listed in Table 1, where m, J, f_{h0}, $f_{\alpha 0}$, ξ_{h0}, and $\xi_{\alpha 0}$ are the inertial mass, initial moment, vertical natural frequency, torsional natural frequency, vertical structural damping, and torsional structural damping of the dynamic system, respectively.

1.2 Flow measurement

Flow measurement around the rectangular flat plate during flutter was performed by two-dimensional PIV techniques. The flow images at the mid-span of the plate were acquired by two high-speed charge-coupled device (CCD) cameras (PCO Dimax HS4) and a 100 mJ double-pulsed laser generator (Beamtech Vlite 430) with two laser paths. The set of PIV devices allows flow measurement with a maximum duration of approximately 40 s under spatial resolutions of 2 200 × 1 600 pixels and a sampling frequency of 200 Hz. This frequency is suitable for capturing the unsteady flow characteristics of nonlinear flutter with a coupled oscillation frequency of approximately 3.46 Hz. Generally, for a PIV measurement of the flow around a bluff body using a single camera and a single laser plane, the laser plane is shaded by test models so that only one-sided flow field can be obtained. Meanwhile, the mid-span flow field near an oscillating model wall with a large amplitude is also shaded by the spanwise end of the test models because of the space perspective relationship. To solve this problem and obtain the complete flow characteristics around the rectangular flat plate, two cameras and two laser beams, as shown in Fig. 2, were used to measure the one-sided flow field around the plate synchronously. The domain sizes of flow measurement on the top and bottom of the model were 320 mm × 240 mm and 380 mm × 280 mm, respectively, and the corresponding spatial accuracies were approximately 0.145 and 0.172 mm/pixel, respectively. The flow-field velocity vectors were calculated from a pair of adjacent snapshots within a given small time interval based on a multiframe cross-correlation algorithm. The size of the interrogation window was set to

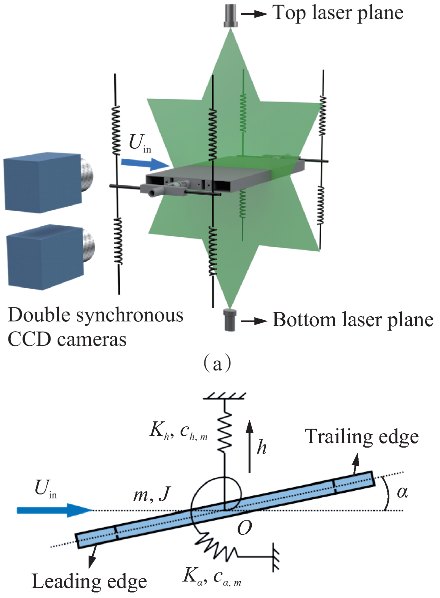

(a)

(b)

Fig. 1 Schematic of the experimental setup. (a) Flow measurement by a PIV technique; (b) Two-degree-of-freedom spring-suspended model

Table 1 Structural dynamic parameters of the spring-suspended section model

H/ mm	B/ mm	m/ kg	J/ (kg·m^2)	f_{h0}/ Hz	$f_{\alpha 0}$/ Hz	ξ_{h0}/ %	$\xi_{\alpha 0}$/ %
30	240	4.17	0.017 9	2.69	3.61	0.23	0.66

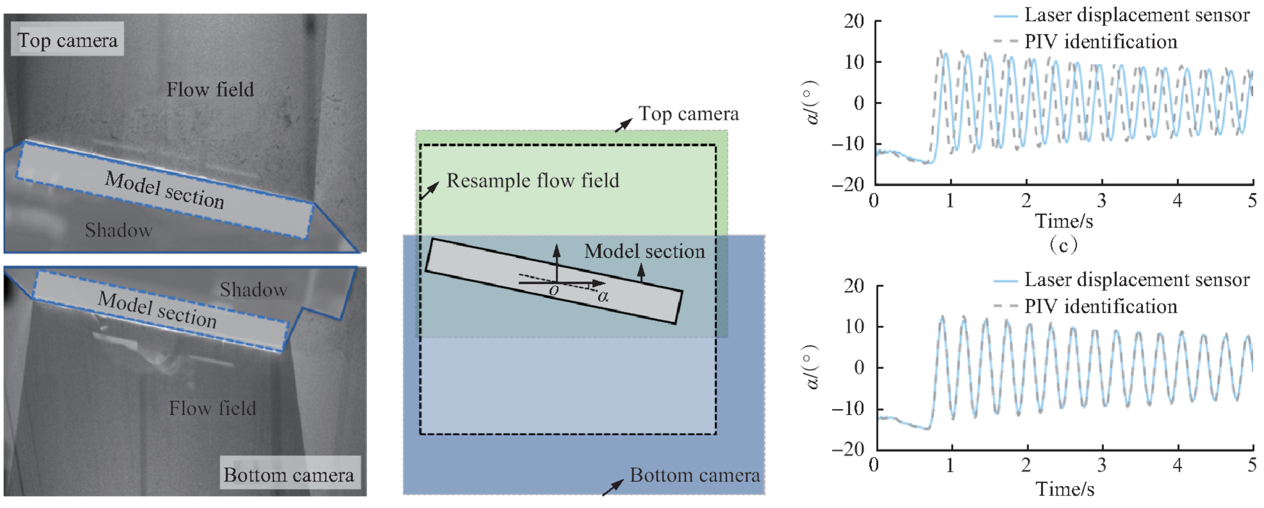

(a) (b) (d)

Fig. 2 Flow chart of reconstruction of the complete flow field around the model based on data from two synchronous cameras. (a) Two-sided PIV images; (b) Same reference frame of the structure; (c) Before phase correction; (d) After phase correction

32 × 32 pixels, and the overlap rate was set to 50% to identify the velocity vectors.

To acquire the complete flow field around the rectangular flat plate, the two cameras were controlled by the synchronous pulse signals from the same pulse generator to simultaneously acquire the two-sided PIV images around the plate. Then, a stitching technique was applied to reconstruct the velocity field based on the same reference frame of the structure in the simultaneous PIV images. The model boundaries were identified as a basic reference object in the two PIV images, and then, a global coordinate system was determined. The locations of these velocity vectors in both PIV images were transformed into the global coordinate system. Finally, the complete velocity field around the rectangular flat plate was obtained for a uniform grid by applying a spline interpolation and resampling method based on the flow data from different cameras.

To accurately and simultaneously determine the oscillation responses and flow fields, the displacement laser sensors and the PIV devices were controlled and preliminarily synchronized by a series of synchronous pulse signals transmitted by a digital delay generator (Berkeley Nucleonics Model 577). Displacement identification based on optical noncontact measurement methods has been widely applied in the field of bridges[40-41]. This method can be used to calibrate vibration signals obtained by PIV image recognition. Further, to calibrate the signal delay induced by the internal circuit differences of different devices, the torsional displacements identified from the model boundary motion in the PIV images were compared with the results from the displacement laser sensors. The signal lag between the data from the two sets of devices was eliminated via a displacement correlation analysis.

1.3 Flutter test results

The flutter instability of the given rectangular flat plate was tested at different inflow velocities. Knowledge of the entire flutter process, including growth stages, decay stages, and steady LCOs, is necessary for exploring the nonlinear characteristics of flutter under bluff aerodynamic configurations. At each wind speed, two excitation conditions, namely, a large-amplitude excitation and no excitation, were separately applied to the model, and the oscillation responses and flow field around the model were measured synchronously.

An example of flutter responses induced by different excitations at $U_{\mathrm{in}}/(f_{\alpha 0}B) = 8.71$ is shown in Fig. 3. The relationship between the root mean square (RMS) of the normalized stable amplitude responses and the reduced wind speeds is shown in Fig. 4(a). For the 8∶1 rectangular flat plate, a nonlinear flutter with LCOs occurs as the inflow velocity exceeds a critical reduced wind speed $U_{\mathrm{in}}/(f_{\alpha 0}B) = 6.04$. Ultimately, the nonlinear oscillation tends to the same stable amplitude regardless of whether the initial excitation is small or large. This is in remarkable contrast with the rapid divergent oscillation of the classical linear flutter. A vertical-torsional coupled phenomenon is observed in the power spectrum shown in Fig. 3. The coupled flutter frequency of $f_c = 3.46$ Hz is closer to the torsional natural frequency $f_{\alpha 0} = 3.61$ Hz than to the vertical natural frequency $f_{h0} = 2.69$ Hz. Similarly, a vertical-torsional amplitude ratio at different inflow velocities is shown in Fig. 4(b); this figure demonstrates that compared to the vertical mode, the torsional mode plays a much more important role in the coupling vibration for the flutter behaviors of an 8∶1 rectangular flat plate.

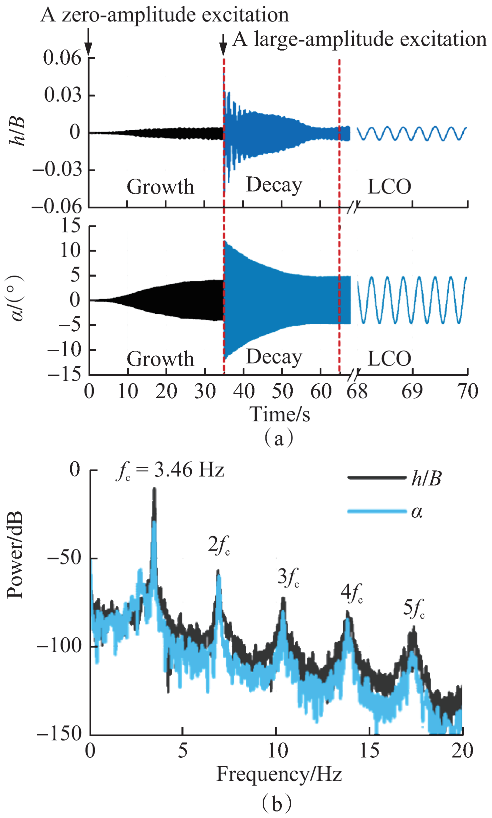

(a)

(b)

Fig. 3 Flutter response histories and power spectra under different initial excitations at $U_{in}/(f_{\alpha0}B) = 8.71$. (a) Flutter response histories; (b) Power spectra

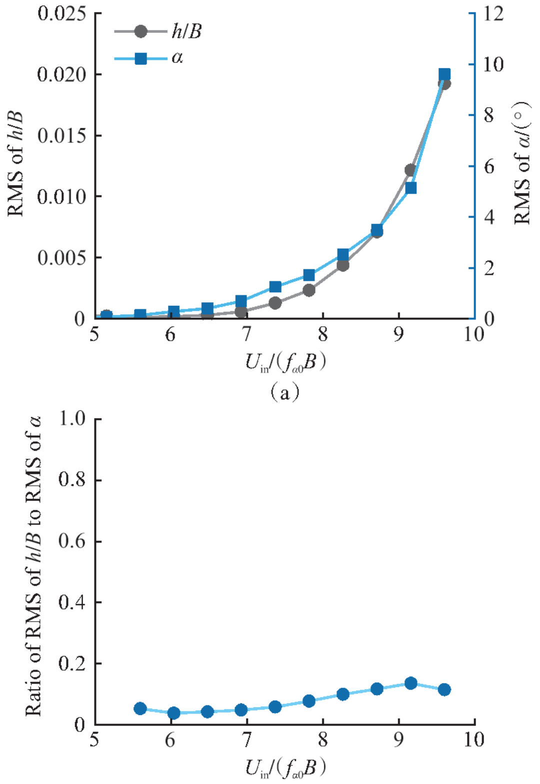

(a)

(b)

Fig. 4 Relationship between the flutter responses and the reduced wind velocity. (a) Stable oscillation amplitude; (b) Amplitude ratio

2 Flow Analysis Method

A major problem in the unsteady flow analysis of flutter is the extraction of the flow characteristics around a moving model with a time-varying amplitude. A representative instantaneous flow field around the rectangular flat plate is shown in Fig. 5(a). The flow field around the model exhibits a multiscale flow structure, including a large-scale LEV (originating from the flow separation induced by the bluff configuration and model oscillation) and a broken small-scale vortex (originating from the Kelvin-Helmholtz instability of the separated free shear layer). A primary step in the unsteady flow analysis of flutter is to identify the characteristic flow structure that will play an important role in the flutter. A thorough analysis revealed that the flow patterns remain more or less the same even at an inflow velocity higher than the flutter critical wind speed and that the characteristic flow structure, i. e., the flapping LEVs, will be stimulated only if the model starts to vibrate. The following paragraphs discuss methods to extract the specific flow structure corresponding to the characteristic scale induced by the model oscillation.

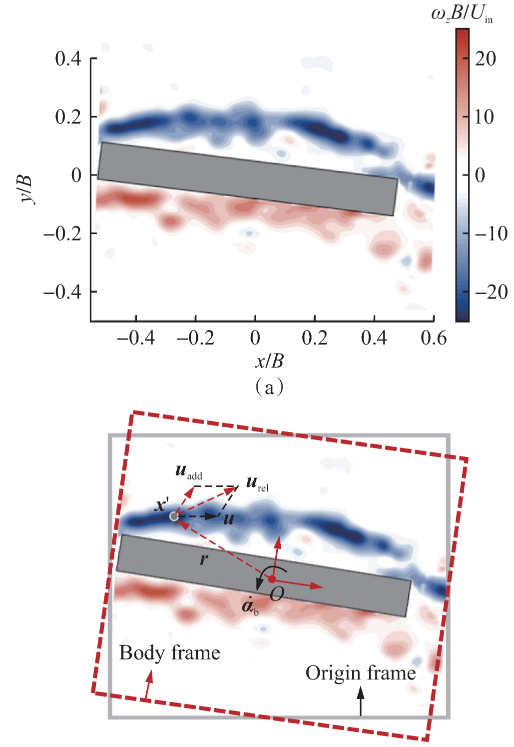

(a)

(b)

Fig. 5 Instantaneous flow field around the rectangular flat plate at $U_{in}/(f_{\alpha0}B) = 8.71$. (a) A snapshot of the vorticity; (b) A schematic diagram of the coordinate transformation in the body frame (taking torsion as an example)

The proper orthogonal decomposition (POD) method introduced by Lumley[42] is the most widely used method to extract coherent structures and to reduce the model order in the flow. POD seeks a series of orthogonal spatial modes to optimally capture the energy feature of the flow data. Nevertheless, the frequency characteristics of the unsteady flow are not considered for space-only POD. The spectral POD (SPOD) method addresses this limitation by solving the eigenvalue problem for a space-time inner product and identifying the modes dependent on both time and space[43]. In previous research, the SPOD method has achieved great success in the low-rank reconstruction and frequency-domain denoising of turbulent flow[44], which can extract the flow structure corresponding to the specific frequency range. Another choice is the phase average method, which is typically used to process periodic unsteady flows. There are many instantaneous flow realizations in different cycles corresponding to the same phase in long-term flow data with numerous repeated cycles. The phase-averaged flow field can be acquired by calculating the average values of these instantaneous flow realizations. However, the original SPOD method and phase average method are not applicable to the flow analysis around the model at growth stages and decay stages of nonlinear flutter because of the time-varying oscillation amplitude. The flow characteristics around the moving model are different for different maximum oscillation amplitudes. Therefore, there is an urgent need to devise an appropriate method to extract the flow characteristics of a moving model with a time-varying amplitude.

Against this background, an extension of the SPOD method in the noninertial frame was proposed. It will be explained in detail in the following section. An SPOD-based reconstructed vorticity field around the moving model was compared with the original and phase-averaged vorticity field to verify the effectiveness of the extended method on extracting the characteristic flow structure for a moving boundary.

2.1 Proper orthogonal decomposition

A flow variable $\boldsymbol{q}(\boldsymbol{x}, t)$ in a flow field can be decomposed into the mean and fluctuation components,

$$\boldsymbol{q}(\boldsymbol{x}, t) = \bar{\boldsymbol{q}}(\boldsymbol{x}) + \boldsymbol{q}'(\boldsymbol{x}, t) \tag{1}$$

where $\boldsymbol{x}$ represents the spatial coordinates; t is time; $\bar{\boldsymbol{q}}(\boldsymbol{x})$ is the average field of $\boldsymbol{q}(\boldsymbol{x}, t)$; and $\boldsymbol{q}'(\boldsymbol{x}, t)$ is the fluctuation component of $\boldsymbol{q}(\boldsymbol{x}, t)$. The POD method aims to find a series of spatial mode functions $\boldsymbol{\phi}(\boldsymbol{x})$ to acquire the best approximation in capturing the energy of $\boldsymbol{q}'(\boldsymbol{x}, t)$. The goal of POD can be formalized by solving the Fredholm eigenvalue problem

$$\int_{\Omega} \boldsymbol{C}(\boldsymbol{x}, \boldsymbol{x}')\boldsymbol{\phi}(\boldsymbol{x}')\mathrm{d}\boldsymbol{x}' = \lambda\boldsymbol{\phi}(\boldsymbol{x}) \tag{2}$$

where Ω is the whole flow domain; $\boldsymbol{C}(\boldsymbol{x}, \boldsymbol{x}') = E\{\boldsymbol{q}'(\boldsymbol{x}, t)\boldsymbol{q}'^{*}(\boldsymbol{x}', t)\}$ is the two-point spatial correlation tensor, and the asterisk superscript denotes the complex conjugate of a scalar or the Hermitian transpose of a vector or tensor. There exists a set of eigenmodes $\{\boldsymbol{\phi}_i(\boldsymbol{x}), \lambda_i\}$ satisfying Eq. (2), where λ_i is the eigenvalue corresponding to the i-th POD mode $\boldsymbol{\phi}_i(\boldsymbol{x})$. The eigenmodes $\{\boldsymbol{\phi}_i(\boldsymbol{x}), \lambda_i\}$ are ranked by the values of λ_i, i.e., $\lambda_1 \geqslant \lambda_2 \geqslant \cdots \geqslant 0$, whose eigenvectors are orthogonal to each other, satisfying the relation $\int_{\Omega} \boldsymbol{\phi}_j^{*}(\boldsymbol{x})\boldsymbol{\phi}_i(\boldsymbol{x})\mathrm{d}\boldsymbol{x} = \delta_{ij}$. The orthogonal eigenvectors can be used as a complete basis, and the $\boldsymbol{q}'(\boldsymbol{x}, t)$ can be expanded as

$$\boldsymbol{q}'(\boldsymbol{x}, t) = \sum_{i=1}^{\infty} a_i(t)\boldsymbol{\phi}_i(\boldsymbol{x}) \tag{3}$$

where $a_i(t) = \int_{\Omega} \boldsymbol{\phi}_j^{*}(\boldsymbol{x})\boldsymbol{q}'(\boldsymbol{x}, t)\mathrm{d}\boldsymbol{x}$ are the time coefficients corresponding to the i-th POD mode $\boldsymbol{\phi}_i(\boldsymbol{x})$. Then, the flow variable $\boldsymbol{q}(\boldsymbol{x}, t)$ can be reconstructed as

$$\boldsymbol{q}(\boldsymbol{x}, t) = \bar{\boldsymbol{q}}(\boldsymbol{x}) + \sum_{i=1}^{\infty} a_i(t)\boldsymbol{\phi}_i(\boldsymbol{x}) \tag{4}$$

2.2 Spectral proper orthogonal decomposition

There is no meaningful connection between the POD modes and the frequency characteristic of the flow, even though the frequency characteristic is crucial for the flow around bluff bodies with a large-amplitude periodic oscillation. The SPOD method provides a feasible algorithm to draw the low-rank flow pattern corresponding to the specific frequency ranges, which are in close agreement with the single-frequency-dominant characteristic of nonlinear flutter. Compared with the space-only POD, the SPOD method searches for the mode functions $\boldsymbol{\phi}(\boldsymbol{x}, t)$ dependent on both space and time to acquire the best approximation for capturing energy of the fluctuation component $\boldsymbol{q}'(\boldsymbol{x}, t)$. A similar eigenvalue problem is proposed to solve SPOD modes:

$$\int_{-\infty}^{\infty}\int_{\Omega} \boldsymbol{C}(\boldsymbol{x}, \boldsymbol{x}', t, t')\boldsymbol{\phi}(\boldsymbol{x}', t')\mathrm{d}\boldsymbol{x}'\mathrm{d}t' = \lambda\boldsymbol{\phi}(\boldsymbol{x}, t) \tag{5}$$

where $\boldsymbol{C}(\boldsymbol{x}, \boldsymbol{x}', t, t') = E\{\boldsymbol{q}'(\boldsymbol{x}, t)\boldsymbol{q}'^{*}(\boldsymbol{x}', t')\}$ is the two-point space-time correlation tensor. The time integral is infinite, implying infinite energy in a space-time norm. To solve the problem, a new eigenvalue problem in spectral space can be derived from Eq. (5) by the Fourier transform method. $\boldsymbol{C}(\boldsymbol{x}, \boldsymbol{x}', t, t')$ can be rewritten as $\boldsymbol{C}(\boldsymbol{x}, \boldsymbol{x}', t - t')$, and the cross-spectral density tensor $\boldsymbol{S}(\boldsymbol{x}, \boldsymbol{x}', f)$ can be calculated by performing a Fourier transform:

$$\boldsymbol{S}(\boldsymbol{x}, \boldsymbol{x}', f) = \int_{-\infty}^{\infty} \boldsymbol{C}(\boldsymbol{x}, \boldsymbol{x}', \tau)\mathrm{e}^{-\mathrm{i}2\pi f\tau}\mathrm{d}\tau \tag{6}$$

where $\tau = t - t'$ is the time difference. A set of spectral eigenvalue problems for an arbitrary given frequency f can be obtained as follows:

$$\int_{\Omega} \boldsymbol{S}(\boldsymbol{x},\boldsymbol{x}',f)\boldsymbol{\psi}(\boldsymbol{x}',f)\mathrm{d}\boldsymbol{x}' = \lambda(f)\boldsymbol{\psi}(\boldsymbol{x},f) \tag{7}$$

where $\boldsymbol{\psi}(\boldsymbol{x}',f)$ is the eigenvector with the eigenvalue $\lambda(f)$ corresponding to the spectral eigenvalue problem of given frequency f. Moreover, the eigenvectors of Eqs. (5) and (7) satisfy

$$\boldsymbol{\phi}(\boldsymbol{x},t) = \boldsymbol{\psi}(\boldsymbol{x}',f)\mathrm{e}^{\mathrm{i}2\pi f\tau} \tag{8}$$

The eigenvectors of the spectral eigenvalue problems are still orthogonal to each other for the same frequency, i. e., $\int_{\Omega} \boldsymbol{\psi}_j^*(\boldsymbol{x},f)\boldsymbol{\psi}_i(\boldsymbol{x},f)\mathrm{d}\boldsymbol{x} = \delta_{ij}$. The Fourier realization of the fluctuation part $\boldsymbol{q}'(\boldsymbol{x},t)$ can be expanded as

$$\widehat{\boldsymbol{q}'}(\boldsymbol{x},f) = \sum_{i=1}^{\infty} a_i(f)\boldsymbol{\psi}_i(\boldsymbol{x},f) \tag{9}$$

where $\widehat{\boldsymbol{q}'}(\boldsymbol{x},f) = \int_{-\infty}^{\infty} \boldsymbol{q}'(\boldsymbol{x},\tau)\mathrm{e}^{-\mathrm{i}2\pi f\tau}\mathrm{d}\tau$ is obtained by a Fourier transform of the fluctuation component $\boldsymbol{q}'(\boldsymbol{x},t)$, and $a_i(f) = \int_{\Omega} \boldsymbol{\psi}_i^*(\boldsymbol{x},f)\widehat{\boldsymbol{q}'}(\boldsymbol{x},f)\mathrm{d}\boldsymbol{x}$ are the expanded coefficients.

Similar to POD, the first few SPOD modes at each frequency are the most energetic and contain most of the information about the flow characteristics for the given frequency. Low-rank, high-fidelity flow reconstruction can be easily achieved by removing the redundant modes with little energy. Furthermore, the flow features corresponding to a specific frequency range can also be handily accessed by bandpass filtering, which is achieved quickly by setting the expanded coefficients $a_i(f)$ as zero for the ineffective frequency range. In practice, low-rank, high-fidelity flow reconstruction $\boldsymbol{q}'_{\mathrm{rec}}(\boldsymbol{x},t)$ for the relevant frequency range can be calculated using an inverse Fourier transform as

$$\boldsymbol{q}'_{\mathrm{rec}}(\boldsymbol{x},t) = \int_{f_1}^{f_2}\left(\sum_{i=1}^{N_{\mathrm{mode}}} a_i(f)\boldsymbol{\psi}_i(\boldsymbol{x},f)\right)\mathrm{e}^{\mathrm{i}2\pi ft}\mathrm{d}f \tag{10}$$

where $[f_1, f_2]$ is the relevant frequency range, and N_{mode} is the truncated mode number at a given frequency f.

2.3 Reconstruction in a noninertial coordinate system

Since flutter is an unsteady fluid-structure interaction phenomenon, its amplitude in the development or decay stages is unstable. Flow reconstruction around the oscillating model boundary with a time-varying amplitude is a crucial problem in fluid-structure interaction mechanism analysis of flutter. An Euler description of the problem will transform the material located around the static model from a fluid to a solid as the model oscillates. Hence, the original SPOD method cannot be used for flow reconstruction affected by the moving body boundary in a fixed Cartesian coordinate system. Therefore, a noninertial body-dependent coordinate system shown in Fig. 5(b) was established to acquire the relative flow around the model, which was taken as a static body in this noninertial frame. In the noninertial frame, the mass center of the model (also the center of vertical and torsional vibration) is set as the origin of the coordinates. A body-dependent window is set to keep relative static with the moving model, and a set of new snapshots of the relative flow in the chosen window is rebuilt at each time instance. For the velocity field $\boldsymbol{u}(\boldsymbol{x}',t)$ at any place $\boldsymbol{x}'$ in the relative static window in the noninertial frame, the added flow velocities $\boldsymbol{u}_{\mathrm{add}}(\boldsymbol{x}',t)$ related to the moving model can be represented as

$$\boldsymbol{u}_{\mathrm{add}} = -\dot{\boldsymbol{\alpha}}_{\mathrm{b}} \times \boldsymbol{r} - \dot{\boldsymbol{h}}_{\mathrm{b}} \tag{11}$$

where $\boldsymbol{r}$ is a radius vector from the coordinate origin to $\boldsymbol{x}'$, and ($\dot{\boldsymbol{h}}_{\mathrm{b}}$, $\dot{\boldsymbol{\alpha}}_{\mathrm{b}}$) are the vertical and torsional velocities of the oscillating model, respectively. The directions of these vectors are indicated in Fig. 5(b). The relative flow velocities $\boldsymbol{u}_{\mathrm{rel}}$ can be represented as

$$\boldsymbol{u}_{\mathrm{rel}}(\boldsymbol{x}',t) = \boldsymbol{u}(\boldsymbol{x}',t) + \boldsymbol{u}_{\mathrm{add}}(\boldsymbol{x}',t) \tag{12}$$

The relative vorticity $\boldsymbol{\omega}_{\mathrm{rel}}(\boldsymbol{x}',t)$ in the noninertial frame can be deduced from Eq. (12),

$$\boldsymbol{\omega}_{\mathrm{rel}}(\boldsymbol{x}',t) = \nabla \times \boldsymbol{u}_{\mathrm{rel}}(\boldsymbol{x}',t) = \nabla \times \boldsymbol{u}(\boldsymbol{x}',t) + \nabla \times \boldsymbol{u}_{\mathrm{add}}(\boldsymbol{x}',t) = \boldsymbol{\omega}(\boldsymbol{x}',t) - 2\dot{\boldsymbol{\alpha}}_{\mathrm{b}} \tag{13}$$

where $\boldsymbol{\omega}(\boldsymbol{x}',t)$ is the absolute vorticity at $\boldsymbol{x}'$, and $-2\dot{\boldsymbol{\alpha}}_{\mathrm{b}}$ is the added vorticity related to the moving model. From the snapshots of the relative flow velocities in a relative static window, the velocities can be reconstructed as $\boldsymbol{u}_{\mathrm{rel,\ rec}}(\boldsymbol{x}',t)$ using the SPOD method by a mode truncation and frequency bandpass filtering according to Eqs. (5)-(10). Then, a reconstructed velocity field $\boldsymbol{u}_{\mathrm{rec}}(\boldsymbol{x}',t)$ in the noninertial frame can be calculated by deducting the added relative flow velocities $\boldsymbol{u}_{\mathrm{add}}(\boldsymbol{x}',t)$ from $\boldsymbol{u}_{\mathrm{rel,\ rec}}(\boldsymbol{x}',t)$,

$$\boldsymbol{u}_{\mathrm{rec}}(\boldsymbol{x}',t) = \boldsymbol{u}_{\mathrm{rel,\ rec}}(\boldsymbol{x}',t) - \boldsymbol{u}_{\mathrm{add}}(\boldsymbol{x}',t) \tag{14}$$

Now, the flow velocities $\boldsymbol{u}_{\mathrm{rec}}(\boldsymbol{x},t)$ in the inertial frame can be obtained from $\boldsymbol{u}_{\mathrm{rec}}(\boldsymbol{x}',t)$ by coordinate transformation and resampling. A similar treatment can be applied to the vorticity field to obtain the reconstructed vorticity $\boldsymbol{\omega}_{\mathrm{rec}}(\boldsymbol{x},t)$ based on a SPOD decomposition of the relative vorticity $\boldsymbol{\omega}_{\mathrm{rel}}(\boldsymbol{x}',t)$.

2.4 Example of flow reconstruction using SPOD

To verify the effectiveness of the SPOD method, the reconstructed vorticity fields around the moving model using the SPOD method and phase-averaging are shown in Fig. 6. All the snapshots of the whole oscillation histories shown in Fig. 6(a) were used to calculate the reconstructed vorticity fields based on the SPOD method. In

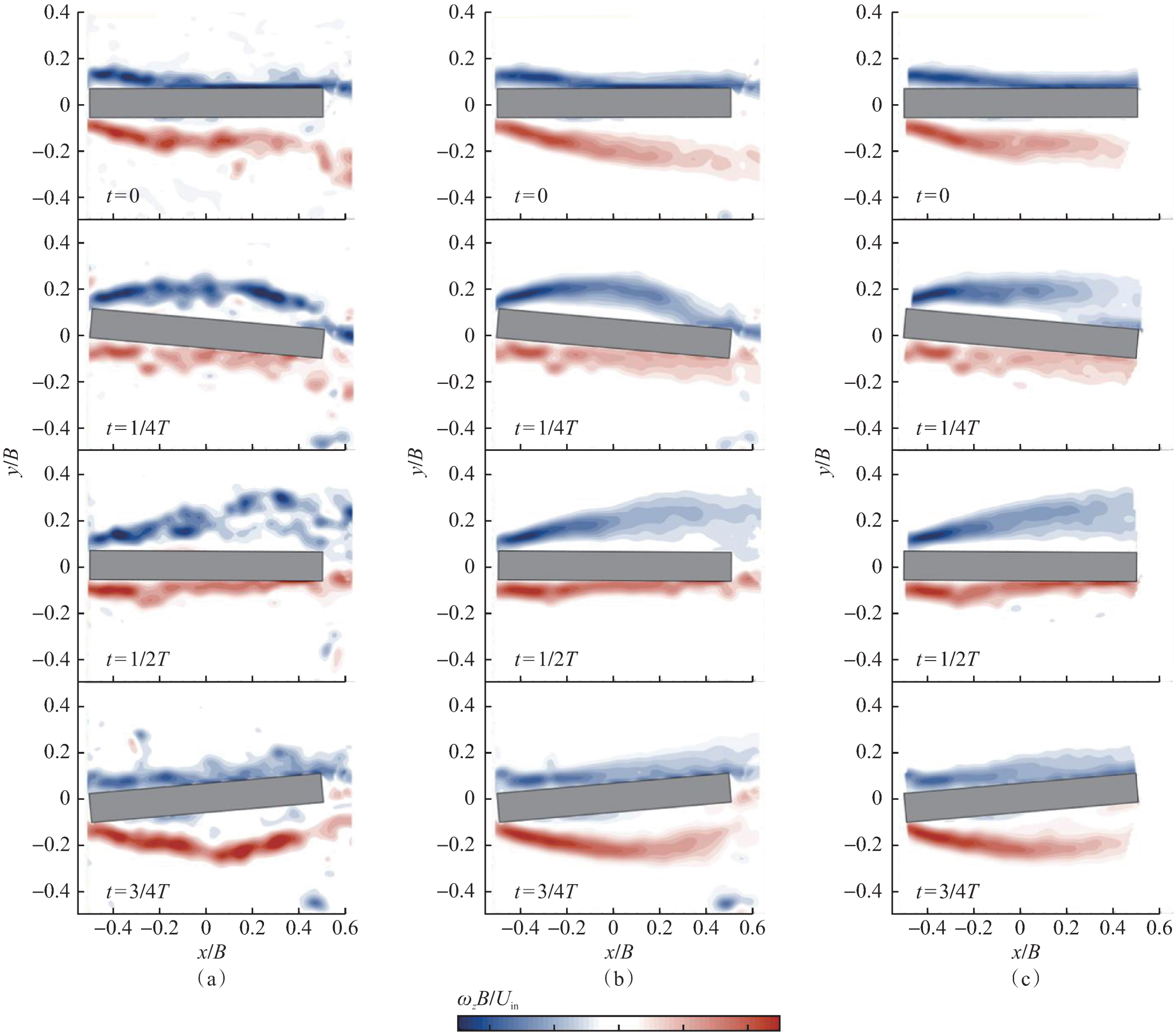

Fig. 6 Comparison of the instantaneous, phase-averaging, and SPOD-based reconstructed vorticity fields in an oscillation period at $U_{in}/(f_{\alpha0}B) = 8.71$. (a) Origin; (b) Phase average; (c) SPOD reconstruction

the SPOD reconstruction, the chosen frequency range $[f_1, f_2]$ was 0-8 Hz, and the truncated mode number N_{mode} was 10. The snapshots, including 54 oscillation periods of the stable-amplitude LCOs, were chosen for phase averaging. In Fig. 6(b), the SPOD-based reconstructed vorticity fields in the first period of the stable-amplitude LCOs were compared with the phase-averaging results, revealing high similarity between the two results.

The eigenvalue distribution of the SPOD reconstruction is shown in Fig. 7(a) to verify the reasonableness of the cutoff frequency of $f_{cut} = 8$ Hz and truncated mode number $N_{mode} = 10$. The eigenvalues indicate the relative importance of each SPOD mode, with higher values representing more significant contributions to the flow. The dominant components are primarily concentrated around the coupled frequency of flutter $f_c = 3.46$ Hz. Given this distribution, it is reasonable to select a cutoff frequency of 8 Hz, as it can capture the essential dynamics associated with the flutter behaviors.

Furthermore, the eigenvalues of the SPOD modes within the cutoff frequency of 8 Hz are summed to compute the cumulative contribution fraction for the mode number, as shown in Fig. 7(b). The cumulative contribution fraction of the first 10 modes exceeds 90%. Therefore, the selection of a cutoff frequency of 8 Hz and the truncated mode number 10 is well-supported by the eigenvalue distribution of the SPOD modes, ensuring preservation of the essential coherent structures for further analysis.

Results of further comparison analysis between the traditional POD and SPOD methods are shown in Fig. 8. The truncated mode number N_{mode} was set 10 for POD reconstruction. The results indicate that when reconstructing the vorticity field using the traditional POD method, a high-frequency vortex shedding structure at the tip of the LEV cannot be isolated easily. In contrast, the SPOD reconstruction incorporating a cutoff frequency of 8 Hz can effectively filter out the high-frequency vortex shedding components, capturing only the flow structures

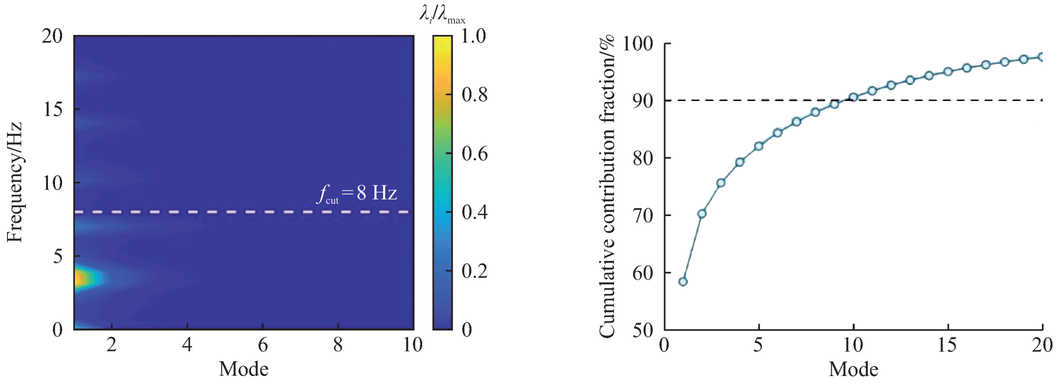

(a) (b)

Fig. 7 Eigenvalue distribution and cumulative contribution fraction of the SPOD modes at $U_{\mathrm{in}}/(f_{\alpha0}B) = 8.71$. (a) Normalized eigenvalue distribution; (b) Cumulative contribution fraction

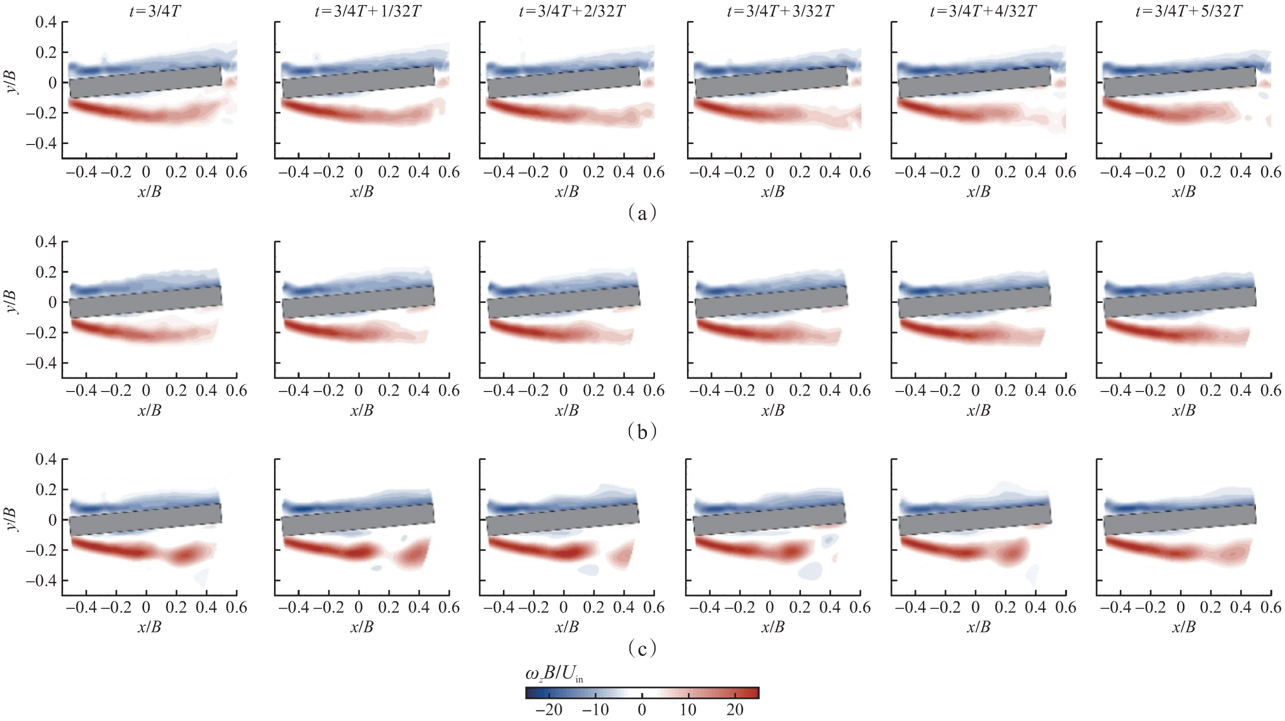

Fig. 8 Comparison of the SPOD-based and POD-based reconstructed vorticity fields in an oscillation period at $U_{\mathrm{in}}/(f_{\alpha0}B) = 8.71$. (a) Phase average; (b) SPOD reconstruction; (c) POD reconstruction

associated with the flutter coupling frequency, i. e., the low-frequency flapping LEV structure. This result clearly demonstrates the effectiveness of the SPOD method in filtering out the high-frequency flow structure and retaining the low-frequency and large-scale vortex induced by the LEV oscillating model.

3 Flutter Mechanism Analysis Considering A Fluid

The unsteady flow around the structure directly and significantly affects the dynamic behaviors of the model. To further explore the detailed flow-structure interaction process and identify the role of unsteady flow in the flutter, two major questions should be addressed: (1) Which characteristic flow structure plays an important role in the flutter? (2) What role does the characteristic flow structure play in the flow-structure interaction process? A series of analysis was performed to answer these questions.

3.1 Flow around the static model

In contrast the case of a low angle of attack, the flow separation around the airfoil with a high angle of attack can cause significant lift reduction. A stall flutter, rather than classical flutter, is induced for such an airfoil. The aerodynamic feature suggests that the flutter characteristics may be related to the flow pattern around the static structure. Similarly, in the present study, the unsteady flow characteristics around the static model were first investigated to determine whether a sudden and vibration-independent alternation occurred in the flow patterns before and after the flutter critical wind speed—such a phenomenon could have been a potential inducement to flutter. A space-only POD method was adopted to extract the characteristic modes of the velocity field nondimensionalized by the inflow velocity around the static model at various wind speeds of $U_{\mathrm{in}}/(f_{\alpha0}B)=5.15$, 6.04 and 8.71, in which $U_{\mathrm{in}}/(f_{\alpha0}B)=6.04$ is close to the flutter critical wind speed. The first few POD modes above the model are shown in Fig. 9, considering the symmetry of the aerodynamic shape. The same-order POD modes differ slightly at different wind speeds, indicating that the flow patterns around the static model do not change as the inflow velocity increases greatly, exceeding the flutter critical wind speed. From the invariance of the flow patterns, it can be inferred that the flow around the static model is not a factor inducing nonlinear flutter.

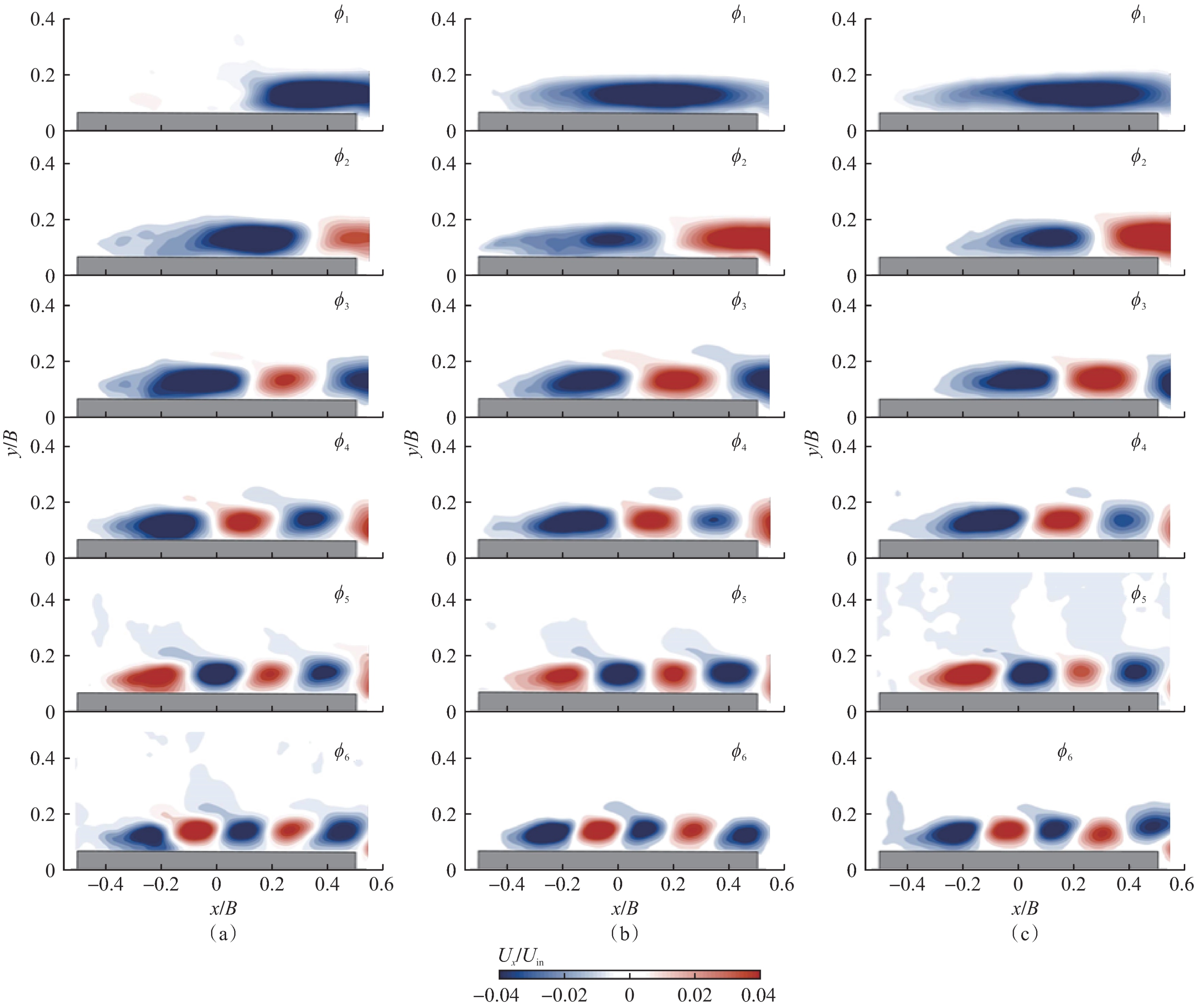

Fig. 9 Comparison of the POD modes of the velocity field around the static model at different inflow velocities. (a) $U_{\mathrm{in}}/(f_{\alpha0}B)=5.15$; (b) $U_{\mathrm{in}}/(f_{\alpha0}B)=6.04$; (c) $U_{\mathrm{in}}/(f_{\alpha0}B)=8.71$

3.2 Flow around the oscillating model

The previous section revealed that no abrupt change occurred in the flow pattern around the pure static model. The result suggests that the model oscillation plays an important role in flutter flow analysis. Next, the flow characteristics influenced by the oscillating model will be a huge focus, and the interaction process between the flow and structural oscillation will be investigated thoroughly.

3.2.1 Time-frequency analysis for an unsteady flow

First, the time-frequency characteristics of the flow field were analyzed for a model with a small-amplitude oscillation. The flow fields around the model with a small torsional amplitude of less than 1° were chosen to analyze the time-frequency characteristics based on a wavelet transform method using the Morlet wavelet. A set of probes was placed in the flow domain above the model only, considering the symmetry of the aerodynamic shape. The distance between two adjacent probes was set as $L=B/20$, and the bottom probe row was installed at $L/2$ above the model boundary to avoid the overlapping between the flow probes and the solid boundary due to model oscillation. The velocities of all the probes, sampled by the PIV tests with a sampling frequency of 200 Hz, were used for the wavelet transform at various inflow velocities $U_{\text{in}}/(f_{\alpha0}B)=5.15$, 6.04 and 8.71. The detailed probe locations are shown in Fig. 10(a). The corresponding torsional oscillation histories at these wind speeds are shown in Figs. 10(b) to (d). The time-frequency results of velocities at three representative locations—probe P1 near the leading edge, probe P2 at the middle reach, and probe P3 near the trailing edge—are shown in Figs. 11-13.

Figs. 11-13 shows that a dominant frequency, coinciding with the oscillation frequency, emerges in the flow near the leading edge when the model vibrates with a small amplitude at different inflow velocities for three given cases. For $U_{\text{in}}/(f_{\alpha0}B)=5.15$, when the vibration amplitude decreases, the dominant frequency of the unsteady flow near the leading edge gradually weakens but still exists at a very low amplitude. The case of $U_{\text{in}}/(f_{\alpha0}B)=6.04$ is very close to the critical state of flutter, and an indistinct dominant frequency also appears in the flow near the leading edge when the oscillation gradually develops and attains a relatively stable amplitude of approximately 0.12°. As the flow develops downstream along the model boundary, the high-frequency fluctuation component of the flow is enhanced remarkably, and the dominant frequency vanishes at P2 and P3. For $U_{\text{in}}/(f_{\alpha0}B)=8.71$, the dominant frequencies of the unsteady flow at P1, P2, and P3 became increasingly significant as the torsional amplitude increased. In general, the dominant flow frequency can be stimulated by model oscillation regardless of whether the inflow velocity exceeds the critical value. The value of the dominant frequency depends on the torsional amplitude and the location relative to the model. A location nearer the leading edge and a larger torsional amplitude favor a higher dominant frequency. Further, it is inferred that the dominant frequency of the downstream flow will be disturbed and unstable because of the effect of shear layer instability.

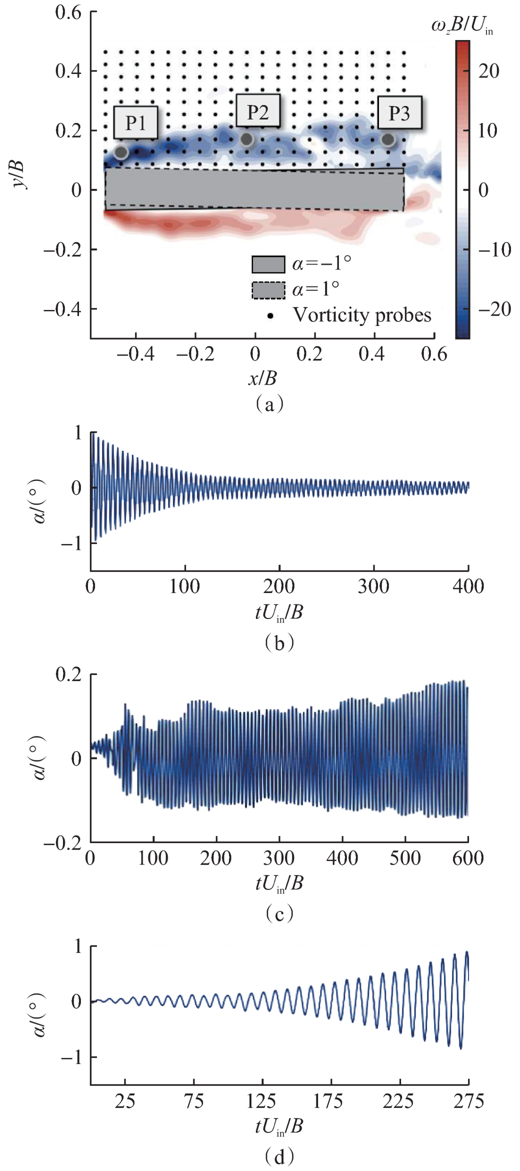

(a)

(b)

(c)

(d)

Fig. 10 Distributions of the probe velocities and oscillation histories corresponding to the wavelet-analysis cases. (a) Velocity probe locations; (b) $U_{\text{in}}/(f_{\alpha0}B)=5.15$; (c) $U_{\text{in}}/(f_{\alpha0}B)=6.04$; (d) $U_{\text{in}}/(f_{\alpha0}B)=8.71$

The time-frequency results for the high-frequency range are also shown in Fig. 11. The distributions of the high-frequency components for various inflow velocities show almost no difference, except for a fluctuation enhancement in the middle and downstream flows. The result indicates that the small-scale flow structure weakly affects flutter behaviors.

3.2.2 Leading-edge flow structure

The time-frequency analysis for the unsteady flow near the model revealed that a characteristic frequency appears in the leading-edge flow when the model starts vibrating. This frequency indicates that a flap of the LEVs can be stimulated by model oscillation, as shown in Fig. 6. Obviously, the LEV flap frequency is identical to the flutter coupled frequency. Conversely, the role of the flapping LEVs in the flutter behaviors is yet to be specified. This section details the efforts made to explore the influence of the special flow structure on the model oscillation. These efforts greatly helped to improve our understanding of the flow-structure interaction process.

In general, the aerodynamic force acting on the model depends strongly on the local flow structure, such as flow separation and vortex motion—both of which are associated with strong vorticity. In vorticity dynamics, the force acting on the body due to the external flow can be

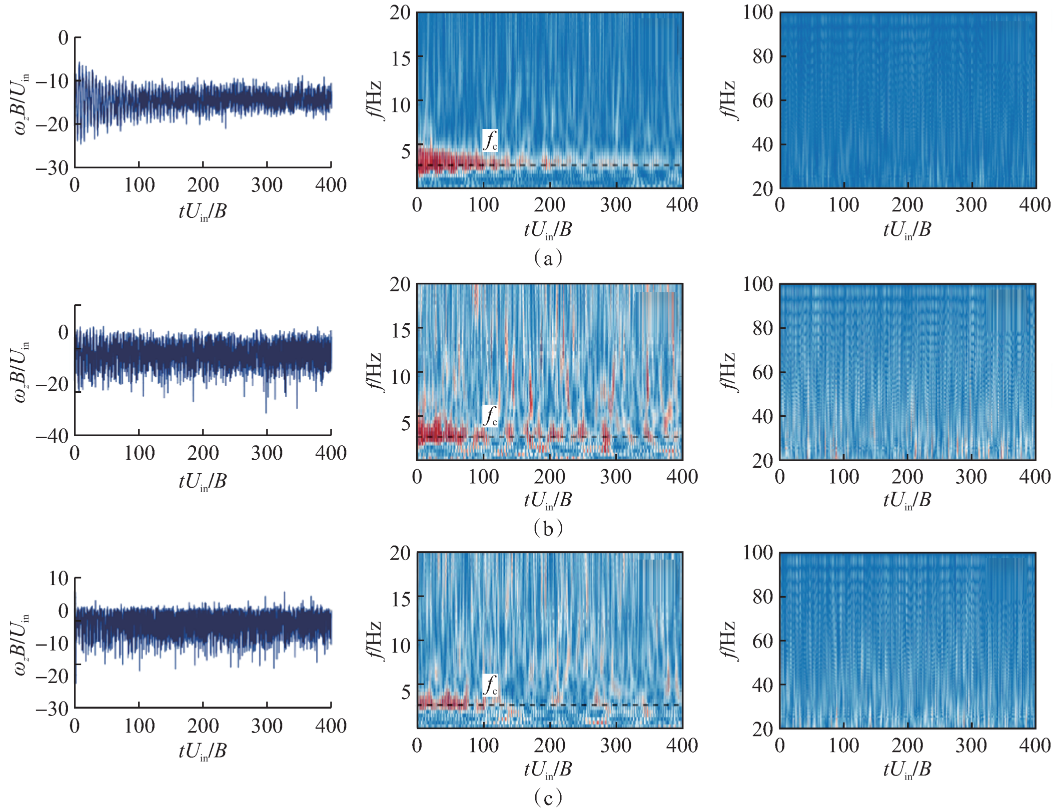

Fig. 11 Time-frequency results of velocity probes at $U_{in}/(f_{\alpha 0}B) = 5.15$. (a) P1; (b) P2; (c) P3

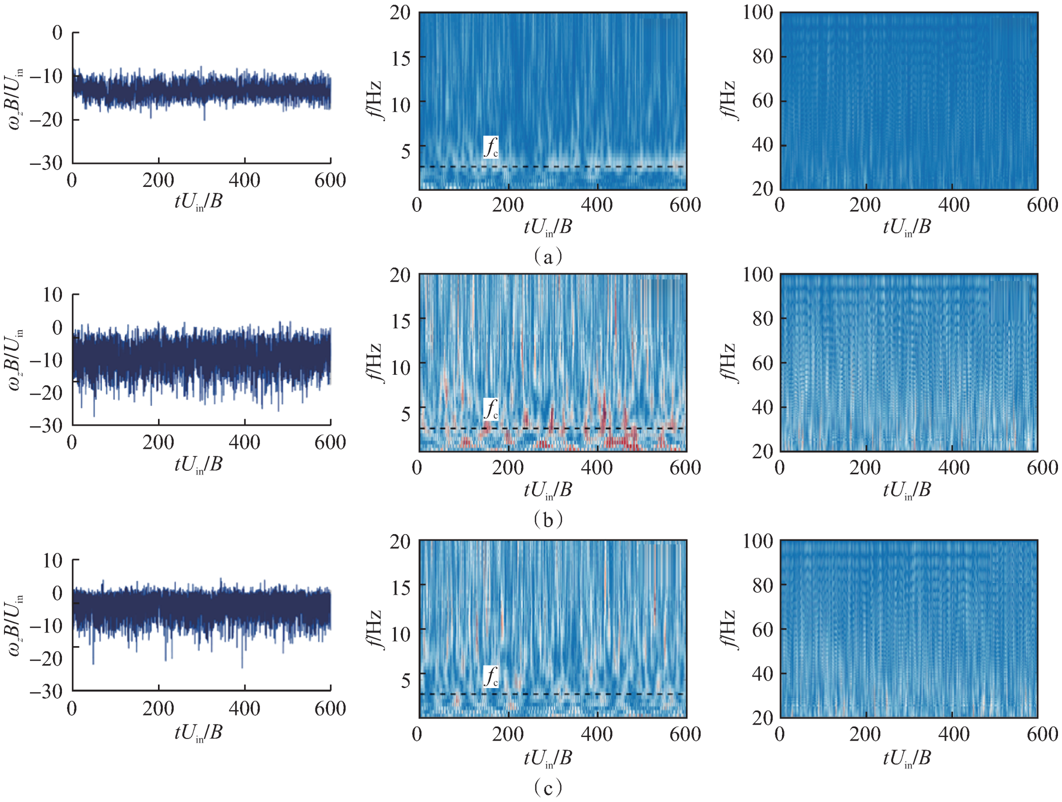

Fig. 12 Time-frequency results of velocity probes at $U_{in}/(f_{\alpha 0}B) = 6.04$. (a) P1; (b) P2; (c) P3

deduced quantitively from a vorticity-related expression[45-46]. Therefore, considering the inherent connection between the vorticity and force, vorticity is chosen as a characteristic physical quantity for the analysis.

For various wind speeds, a series of specific vibration amplitudes ranging 1°-10° and an interval of 1° were chosen. A slice of one-cycle response history corresponding to the given amplitudes was extracted from the growing

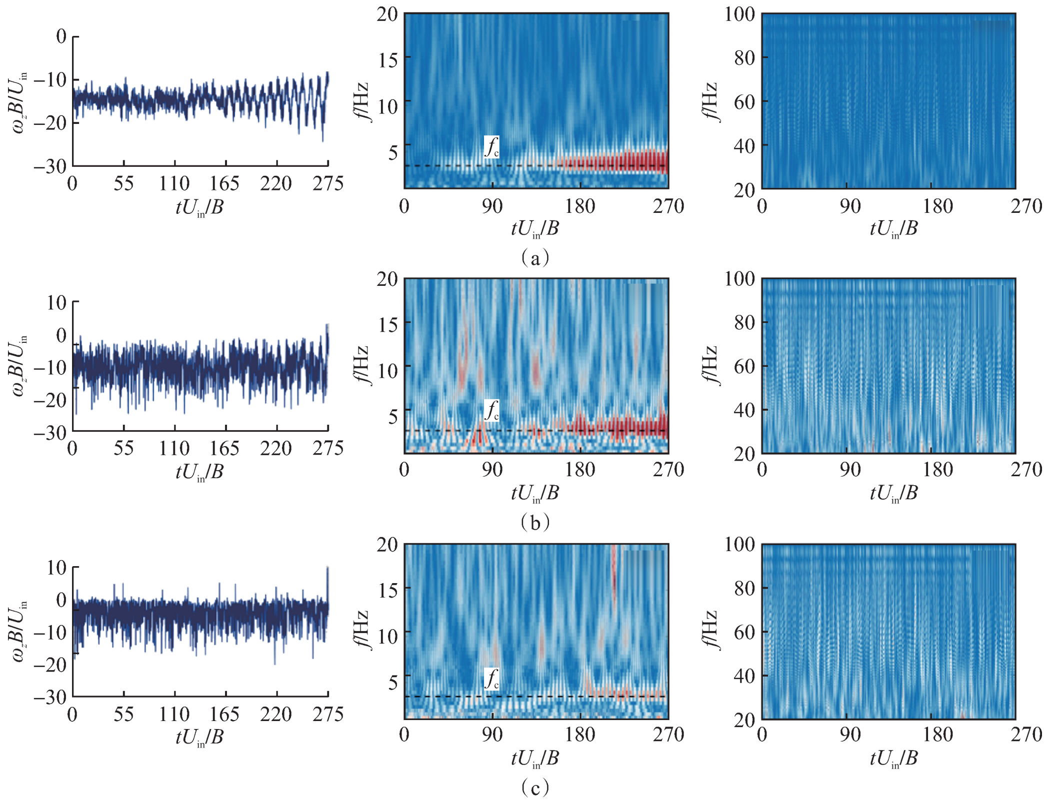

Fig. 13 Time-frequency results of velocity probes at $U_{in}/(f_{\alpha 0}B) = 8.71$. (a) P1; (b) P2; (c) P3

or decay flutter response signals. While the flutter responses may continue to grow or decay at the given amplitude for different inflow velocities, the flow states during the period of oscillation can be considered to be unaffected by the previous oscillation due to the slowly varying nonlinearity. The synchronous snapshots of the vorticity fields in the period of oscillation were acquired. The SPOD method (see Section 2) was used to reconstruct the low-rank, high-fidelity vorticity field corresponding to the characteristic frequency. The low-pass cutoff frequency was set to $f_{cut} = 8$ Hz. The truncated order of SPOD modes at each frequency component was set to $N_{mode} = 10$. The reconstructed dimensionless vorticity fields at different inflow velocities are listed in Figs. 14 and 15, in which the dash line represents the isopleth of $\omega_z B/U_{in} = \pm 5$.

When the model remains static, as shown in Fig. 14, a couple of LEVs are produced symmetrically at both sides of the leading edge because of the flow separation. The LEVs are distributed along the model boundary with a size similar to the model width. As the oscillation amplitude gradually increases, the couple of LEVs shown in Fig. 15 start to flap in the opposite phase because of the model oscillation. When the model is located at the equilibrium position $\alpha = 0°$ and moves to a positive angle of attack, the LEV is induced at the top side of the leading edge. It is enhanced as the model reaches the maximum torsional amplitude. Then, as the model moves and approaches equilibrium again from the torsional peak position, the top-side LEV continues to develop downstream and gradually separates from the model wall at a large torsional amplitude. Before the model vibrates to another torsional peak position corresponding to a negative angle of attack, the top-side LEV starts approaching the model wall and weakens. Similarly, the bottom-side LEV exhibits the same dynamic behavior with an opposite phase compared with the top-side LEV due to the symmetry of the aerodynamic configuration.

An interesting and thought-provoking phenomenon is the distinct difference in vorticity distribution for various inflow velocities, even when the model vibrates in the same phase of the same oscillation period and amplitude. A striking example is that the vorticity distribution above the model at $t = 1/4T$ for $U_{in}/(f_{\alpha 0}B) = 5.15$ is similar to that at $t = 1/8T$ for $U_{in}/(f_{\alpha 0}B) = 6.93$, while the top-side LEVs are generated at the equilibrium position corresponding to $t = 0$. The results show that the evolution of LEV at a low wind speed is slower than that at a higher wind speed, implying that the change in inflow velocity arouses a discrepant interaction effect between the LEV flap and model oscillation.

3.2.3 Correlation analysis of the LEV

To quantitatively evaluate the interaction effect at various inflow velocities, a correlation analysis of the dimensionless vorticity field was performed. The analysis

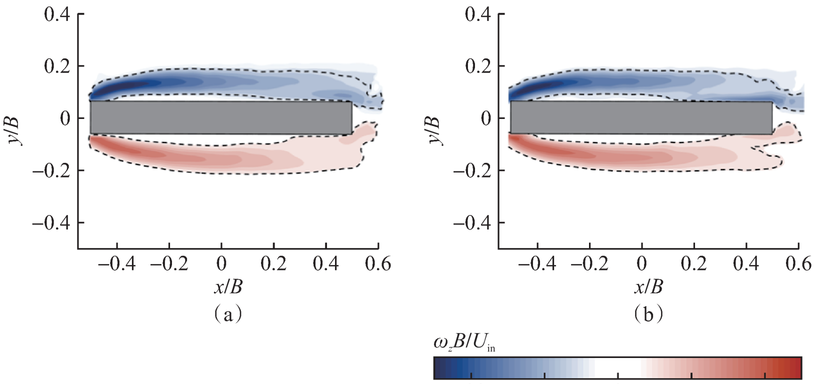

Fig. 14 Nondimensional vorticity distribution around the static model at different inflow velocities. (a) $U_{in}/(f_{\alpha0}B) = 5.15$; (b) $U_{in}/(f_{\alpha0}B) = 6.93$; (c) $U_{in}/(f_{\alpha0}B) = 8.71$

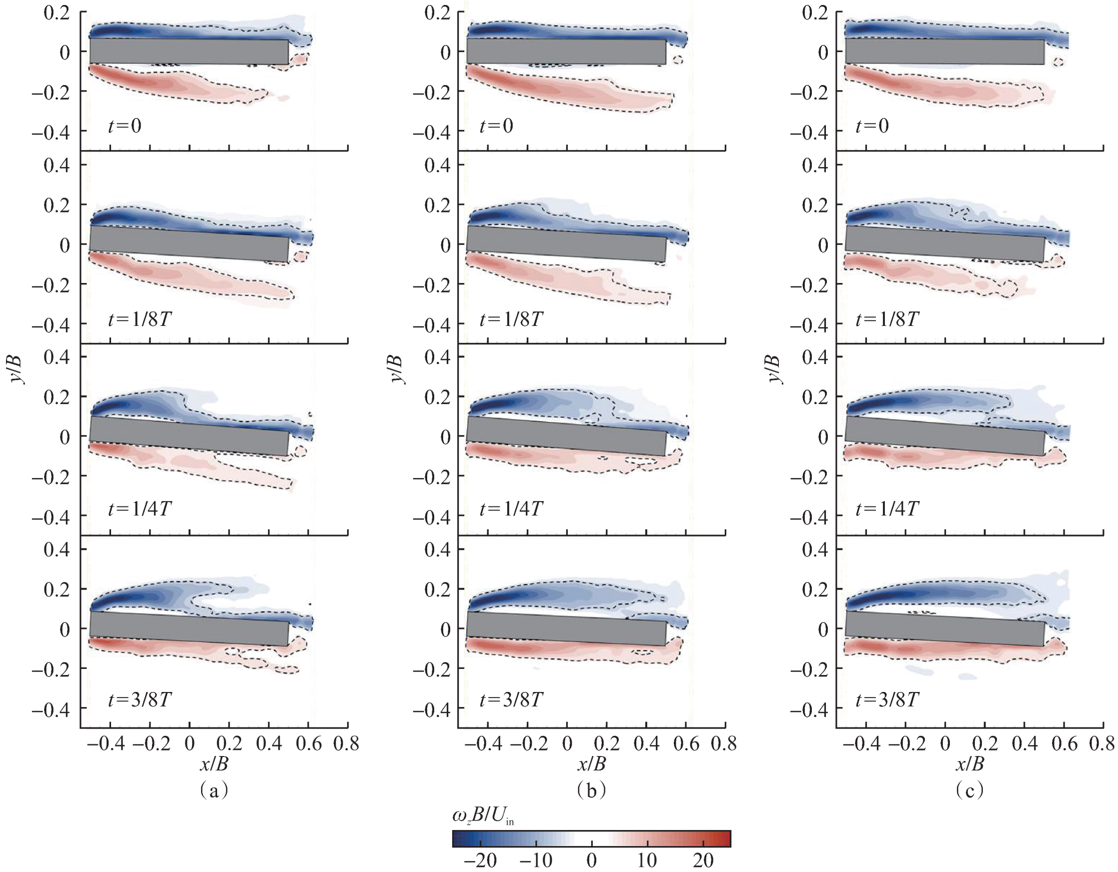

Fig. 15 Nondimensional vorticity distribution in an oscillation period for different inflow velocities ($\alpha_{Amp} = 4°$). (a) $U_{in}/(f_{\alpha0}B) = 5.15$; (b) $U_{in}/(f_{\alpha0}B) = 6.93$; (c) $U_{in}/(f_{\alpha0}B) = 8.71$

yielded the phase lead of the LEV flap at different wind speeds when the model oscillated in the same phase with the same amplitude. A detailed schematic diagram of the correlation analysis and phase-lead calculation for different inflow velocities is shown in Fig. 16.

For all wind speeds, the SPOD-reconstructed dimensionless vorticity field in a period of oscillation with the same amplitude was selected for comparison. $U_{in}/(f_{\alpha0}B) = 5.15$ was taken as a reference case. The snapshots of dimensionless vorticity are denoted as $\{\boldsymbol{\omega}_1, \boldsymbol{\omega}_2, \cdots, \boldsymbol{\omega}_{N_s}\}_{U_{in}=U_{comp}}$ for the cases to be compared and as $\{\boldsymbol{\omega}_1, \boldsymbol{\omega}_2, \cdots, \boldsymbol{\omega}_{N_s}\}_{U_{in}=U_{ref}}$ for the reference case. These vorticity snapshots share a series of identical oscillation phases $\phi_1, \phi_2, \cdots, \phi_{N_s}$ ranging from 0 to 2π, and N_s is the total number of snapshots in a period of oscillation. For the i-th dimensionless vorticity field $\boldsymbol{\omega}_i$ corresponding to a specific phase ϕ_i at other wind speeds, the most relevant vorticity field $\boldsymbol{\omega}_{i'}$ corresponding to phase $\phi_{i'}$ of the reference case is selected based on the criterion

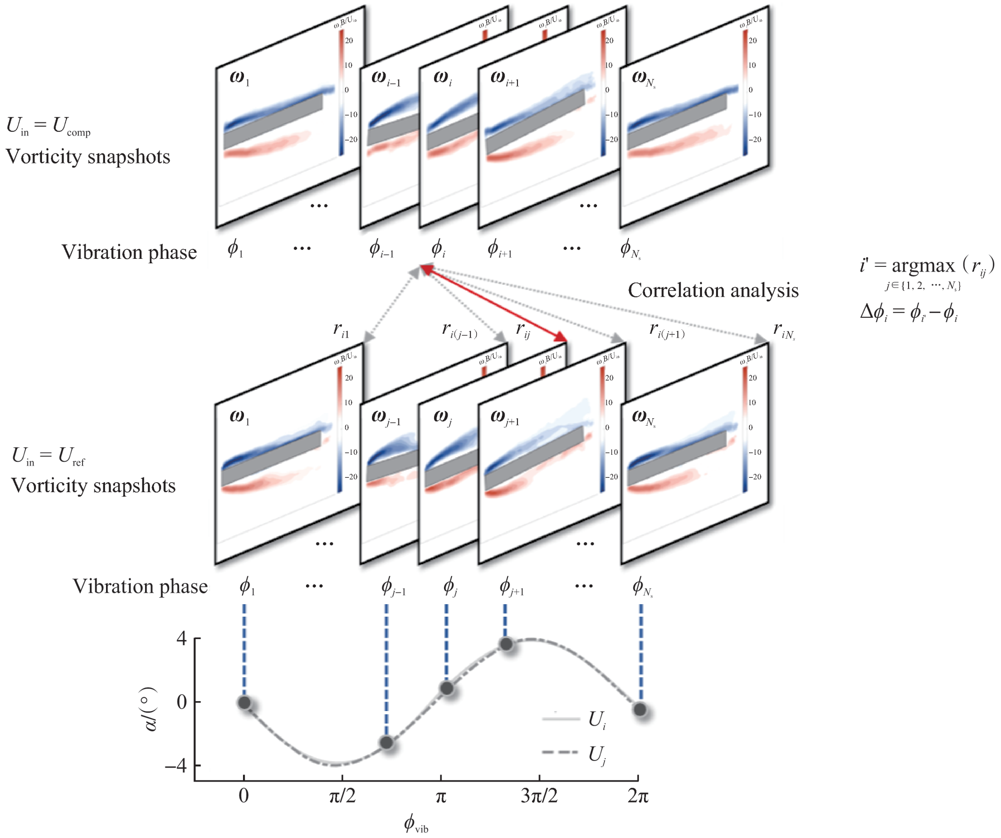

Fig. 16 Schematic diagram of the vorticity-based flow correlation analysis and phase-lead calculation for different inflow velocities

$$i' = \underset{j \in \{1, 2, \cdots, N_s\}}{\mathrm{argmax}} (r_{ij}) \tag{15}$$

A two-dimensional correlation coefficient r_{ij} between two dimensionless vorticity fields $\boldsymbol{\omega}_i$ and $\boldsymbol{\omega}_j$ of is defined as

$$r_{ij} = \frac{\sum_m \sum_n (\boldsymbol{\omega}_i^{mn} - \bar{\boldsymbol{\omega}}_i)(\boldsymbol{\omega}_j^{mn} - \bar{\boldsymbol{\omega}}_j)}{\sqrt{\left(\sum_m \sum_n (\boldsymbol{\omega}_i^{mn} - \bar{\boldsymbol{\omega}}_i)^2\right)\left(\sum_m \sum_n (\boldsymbol{\omega}_j^{mn} - \bar{\boldsymbol{\omega}}_j)^2\right)}} \tag{16}$$

where $m \times n$ are the dimensions of the 2D snapshots of dimensionless vorticity, and the top mark, i. e. , a horizontal line, represents an average value of the 2D snapshots. Then, the phase difference $\Delta\phi_i$ can be calculated by

$$\Delta\phi_i = \phi_{i'} - \phi_i \tag{17}$$

which expresses an oscillation phase difference for two cases of different wind speeds when the vorticity distributions are the most similar for a given oscillation period. A positive $\Delta\phi_i$ means that a similar flow structure will appear at a lead oscillation phase for the case to be compared with the reference. The phase difference $\Delta\phi_i$ provides a quantitative indicator to evaluate the evolution speed difference of the LEV at different inflow velocities when the model vibrates with the same amplitude.

Fig. 17 shows the phase difference $\Delta\phi_i$ for the reference case $U_{in}/(f_{\alpha 0}B) = 5.15$ for two different oscillation amplitudes $\alpha_{max} = 4°$ and $\alpha_{max} = 8°$. The zero phase of oscillation $\phi_i = 0$ represents the equilibrium position tending to a positive angle of attack, corresponding to $t = 0$ in Fig. 15. For all inflow velocities, the phase differences $\Delta\phi_i$ of the vorticity field for the reference case gradually rises until the oscillation phase ϕ_i increases to 180°. In a specific vibration phase, the phase differences $\Delta\phi_i$ at a higher inflow velocity are larger than that at a lower inflow velocity. A larger phase difference indicates the faster development of the LEV flap at a higher wind speed, but in the same oscillation period, which is shown in Fig. 15. Moreover, the phase differences $\Delta\phi_i$ sharply fall to almost 0° when the oscillation phase ϕ_i approaches to 180°. At this moment, the model moves to the equilibrium position from the positive angle of attack. The top-side LEV almost disappears, whereas the bottom-side LEV begins to be induced and enhanced. Therefore, the dramatic slump of the phase differences $\Delta\phi_i$ at about $\phi_i = 180°$ is triggered by the switching of the dominant flow structure from the top-side LEV to the bottom-side LEV.

3.3 Analysis of the fluid-structure interaction mechanism

The relationship between the leading-edge vortex and aerodynamic forces has been extensively studied[33, 35, 46-47]. However, it is challenging to establish a

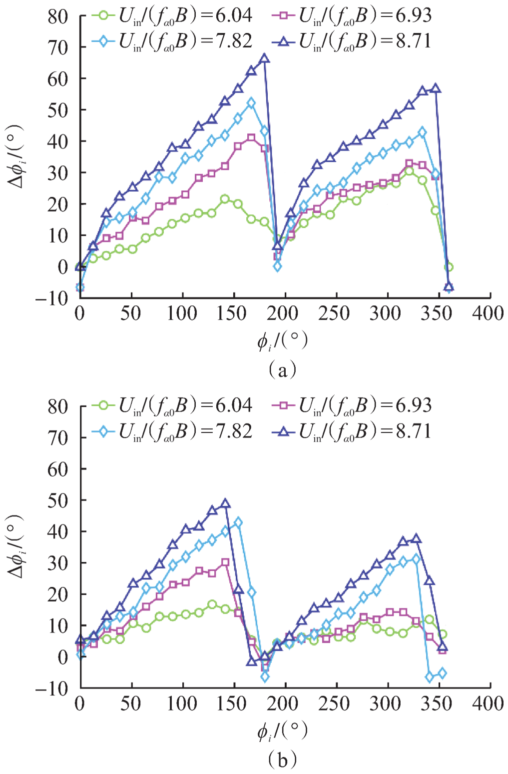

(a)

(b)

Fig. 17 Phase differences $\Delta\phi_i$ versus the oscillation phase ϕ_i for the reference case $U_{in}/(f_{\alpha0}B) = 5.15$ for different inflow velocities. (a) $\alpha_{max} = 4°$; (b) $\alpha_{max} = 8°$

direct quantitative relationship between the two for viscous flows around a bluff body at high Reynolds numbers. Howe[48] and Wu et al. [46] deduced an expression for the aerodynamic force and torque acting on a bluff body for 2D viscous flows, but it is difficult to apply it directly for analysis. However, their results indicate that for a given aerodynamic configuration, a similar flow structure will induce a similar aerodynamic torque. Therefore, in essence, the phase difference $\Delta\phi_i$ can be considered an indicator of the phase differences of aerodynamic torque at different inflow velocities when the oscillation phases remain the same for a period of oscillation.

The relationship between the phase difference of the aerodynamic torque and oscillation and the aerodynamic work can be directly derived from the dynamic equations. For the flutter dynamic system of an 8∶1 rectangular flat plate, the dynamic equation can be simply represented as a single degree-of-freedom torsional motion:

$$J\ddot{\alpha} + c_{\alpha0}\dot{\alpha} + K_{\alpha0}\alpha = T_{se} \tag{18}$$

where T_{se} is aerodynamic torque; J is an inertial moment; $c_{\alpha0}$ and $K_{\alpha0}$ are mechanical damping and stiffness, respectively. The response α can be approximated as a sinusoidal oscillation with an amplitude α_{max} and a flutter frequency ω_c:

$$\alpha = \alpha_{max}\sin(\omega_c t) \tag{19}$$

Further, the aerodynamic torque can be represented as a function of motion states:

$$T_{se} = c_{\alpha,se}\dot{\alpha} + K_{\alpha,se}\alpha = c_{\alpha,se}\alpha_{max}\omega_c\cos(\omega_c t) + K_{\alpha,se}\alpha_{max}\sin(\omega_c t) = T_{max}\sin(\omega_c t + \Delta\varphi_T) \tag{20}$$

where $c_{\alpha,se}$ and $K_{\alpha,se}$ are aerodynamic damping and stiffness, respectively; $T_{max} = \alpha_{max}\sqrt{c_{\alpha,se}^2\omega_c^2 + K_{\alpha,se}^2}$; $\tan\varphi_T = c_{\alpha,se}\omega_c/K_{\alpha,se}$; and the phase $\Delta\varphi_T$ represents a phase difference of the aerodynamic torque T_{se} compared to the torsional angle α. The work P done by the aerodynamic torque is then given as follows:

$$P = \int_0^{\frac{2\pi}{\omega_c}} T_{se}\dot{\alpha}\mathrm{d}t = T_{max}\alpha_{max}\int_0^{\frac{2\pi}{\omega_c}}\sin(\omega_c t + \Delta\varphi_T)\cos(\omega_c t)\mathrm{d}t = \pi T_{max}\alpha_{max}\sin\Delta\varphi_T \tag{21}$$

Note that the sign of P is determined solely by the phase difference $\Delta\varphi_T$ between the aerodynamic torque T_{se} and the response α. As $\Delta\varphi_T$ increases, the work P done by the aerodynamic torque T_{se} changes from negative to positive, inducing an oscillation in the dynamic system.

The increasing $\Delta\phi_i$ signifies an enhanced ability to do work induced by the aerodynamic torque on the structure. Based on the indicator $\Delta\phi_i$, an intuitive physical diagram of the interaction process of the nonlinear flutter of the rectangular flat plate was drawn. The flapping LEVs form a crucial link for energy transfer between the fluid and structure. The oscillation of the model induces flapping of LEVs produced by the flow separation. The flapping frequency is identical to the dominant frequency of model oscillation. Conversely, the LEVs develop faster as the inflow velocity increases, heightening the phase differences between the aerodynamic force and oscillation. The increase in the phase differences allows the fluid around the model to do more work by acting on the structure to induce a flutter behavior.

The LEV evolution process depends on model oscillation. The influence of an increasing wind speed is somewhat homologous to the elevated oscillation frequency for the LEV flap—both result in the faster development of the LEVs downstream in a period of oscillation. Therefore, the relative ratio of the inflow velocity and oscillation frequency should be a control parameter for the nonlinear flutter based on the theory of the flapping LEVs. Coincidentally, the control parameter is consistent with the reduced wind velocity $U_{in}/\omega B$, which is a vital dimensionless independent variable describing the aerodynamic force in Scanlan's classical theory of flutter derivatives, as well as other nonlinear models of aerodynamic force. Thus, the rationality of the interaction mechanism analysis is validated indirectly from the viewpoint of flapping LEVs for the flutter of a rectangular flat plate.

4 Conclusions

The study presents an experimental investigation of the unsteady flow characteristics of flutter instability for a rectangular flat plate with $B/H = 8:1$. Different initial excitations were exerted to obtain the all-around nonlinear dynamic characteristics during the entire flutter process, including the growth stages, decay stages, and steady LCOs. The complete velocity field around the oscillating model was obtained based on a PIV technique using two synchronous cameras and a stitching method. A novel insight into the fluid-structure interaction mechanism of flutter was provided based on a deep understanding of the unsteady flow characteristics around the oscillating model, especially the formation and evolution of flapping LEVs induced by the structure oscillation.

The unsteady flow characteristics around the static and oscillating models were explored using a POD method and wavelet transform analysis, respectively. The flow patterns around the static model remained unchanged regardless of whether the inflow velocity exceeded the flutter critical wind speed. A characteristic frequency identical to the flutter coupled frequency appeared in the flow at the leading edge only if the model started vibrating, indicating the flapping of the LEVs stimulated by the model oscillation.

To acquire the characteristic flow structure for a specific frequency range, the SPOD method was extended in the noninertial frame to reconstruct a low-rank, high-fidelity flow field around the moving model with a time-varying amplitude. The SPOD-based reconstructed vorticity fields were compared with the phase-averaging results. The result indicated that the extended SPOD method filtered out the small and broken high-frequency flow structure and successfully captured the large-scale LEVs induced by model oscillation.

The formation and evolution of the flapping LEVs in an oscillation period were investigated for different inflow velocities based on the SPOD-reconstructed vorticity field. A correlation analysis was performed for the vorticity distributions to quantitatively evaluate the differences in the interaction process between the flow and structure for different inflow velocities. We discovered that the flapping LEVs can build a critical connection for energy transfer between the fluid and structure. A significant phase lead phenomenon was observed in the LEV evolution downstream for a higher inflow velocity, even with the same vibration amplitude. The leading phase of the flow evolution at a higher inflow velocity is related to the expansion of the phase differences between the aerodynamic force and oscillation. The phase offset of the aerodynamic forces allows the flow acting on the structure to do more work, finally resulting in flutter.

References

[1] SCANLAN R H, TOMKO J J. Airfoil and bridge deck flutter derivatives[J]. Journal of the Engineering Mechanics Division, 1971, 97(6): 1717-1737.

[2] MATSUMOTO M. Aerodynamic damping of prisms [J]. Journal of Wind Engineering and Industrial Aerodynamics, 1996, 59(2/3): 159-175.

[3] GU M, ZHANG R X, XIANG H F. Identification of flutter derivatives of bridge decks[J]. Journal of Wind Engineering and Industrial Aerodynamics, 2000, 84(2): 151-162.

[4] CHEN A R, HE X F, XIANG H F. Identification of 18 flutter derivatives of bridge decks[J]. Journal of Wind Engineering and Industrial Aerodynamics, 2002, 90(12/13/14/15): 2007-2022.

[5] XU F Y, ZHU L D, GE X M, et al. Some new insights into the identification of bridge deck flutter derivatives [J]. Engineering Structures, 2014, 75: 418-428.

[6] NIETO F, OWEN J S, HARGREAVES D M, et al. Bridge deck flutter derivatives: Efficient numerical evaluation exploiting their interdependence[J]. Journal of Wind Engineering and Industrial Aerodynamics, 2015, 136: 138-150.

[7] ANDERSEN M S, ØISETH O, JOHANSSON J, et al. Flutter derivatives from free decay tests of a rectangular B/D=10 section estimated by optimized system identification methods[J]. Engineering Structures, 2018, 156: 284-293.

[8] ZHOU R, WANG H, XU Z D. Analysis on flutter performance of flexible photovoltaic support based on full-order method[J]. Journal of Southeast University (English Edition), 2024, 40(3): 238-244.

[9] AMANDOLESE X, MICHELIN S, CHOQUEL M. Low speed flutter and limit cycle oscillations of a two-degree-of-freedom flat plate in a wind tunnel[J]. Journal of Fluids and Structures, 2013, 43: 244-255.

[10] ARENA A, LACARBONARA W, MARZOCCA P. Post-critical behavior of suspension bridges under nonlinear aerodynamic loading[J]. Journal of Computational and Nonlinear Dynamics, 2016, 11: 011005.

[11] MENON K, MITTAL R. Flow physics and dynamics of flow-induced pitch oscillations of an airfoil[J]. Journal of Fluid Mechanics, 2019, 877: 582-613.

[12] ZHOU R, GE Y J, YANG Y X, et al. Wind-induced nonlinear behaviors of twin-box girder bridges with various aerodynamic shapes [J]. Nonlinear Dynamics, 2018, 94(2): 1095-1115.

[13] ZHU Y H, SU Y X, BREUER K. Nonlinear flow-induced instability of an elastically mounted pitching wing[J]. Journal of Fluid Mechanics, 2020, 899: A35.

[14] YUAN W Y, LAIMA S J, CHEN W L, et al. External excitation effects on the flutter characteristics of a 2-DOF rigid rectangular panel[J]. Journal of Wind Engineering and Industrial Aerodynamics, 2021, 209: 104486.

[15] ZHANG H F, WEN J H, ZHOU L. Reduced-order model of unsteady wind turbine wake based on a multifunctional recurrent fuzzy neural network[J]. Journal of

Southeast University (English Edition), 2025, 41(4): 437-445.

[16] ZOU L H, WANG J, SONG J, et al. Analysis of wind-induced vibration response characteristics of multi-span double-layer cable photovoltaic support structure [J]. Journal of Southeast University (English Edition), 2025, 41(1): 37-43.

[17] SCANLAN R H. Amplitude and turbulence effects on bridge flutter derivatives [J]. Journal of Structural Engineering, 1997, 123(2): 232-236.

[18] NODA M, UTSUNOMIYA H, NAGAO F, et al. Effects of oscillation amplitude on aerodynamic derivatives [J]. Journal of Wind Engineering and Industrial Aerodynamics, 2003, 91(1/2): 101-111.

[19] NÁPRSTEK J, POSPÍŠIL S, HRAČOV S. Analytical and experimental modelling of non-linear aeroelastic effects on prismatic bodies [J]. Journal of Wind Engineering and Industrial Aerodynamics, 2007, 95(9/10/11): 1315-1328.

[20] GAO G Z, ZHU L D, HAN W S, et al. Nonlinear post-flutter behavior and self-excited force model of a twin-side-girder bridge deck [J]. Journal of Wind Engineering and Industrial Aerodynamics, 2018, 177: 227-241.

[21] GAO G Z, ZHU L D, LI J W, et al. A novel two-degree-of-freedom model of nonlinear self-excited force for coupled flutter instability of bridge decks [J]. Journal of Sound and Vibration, 2020, 480: 115406.

[22] WU B, WANG Q, LIAO H L, et al. Hysteresis response of nonlinear flutter of a truss girder: Experimental investigations and theoretical predictions [J]. Computers & Structures, 2020, 238: 106267.

[23] ZHANG M J, XU F Y, ZHANG Z B, et al. Energy budget analysis and engineering modeling of post-flutter limit cycle oscillation of a bridge deck [J]. Journal of Wind Engineering and Industrial Aerodynamics, 2019, 188: 410-420.

[24] WU B, WANG Q, LIAO H L, et al. Flutter derivatives of a flat plate section and analysis of flutter instability at various wind angles of attack [J]. Journal of Wind Engineering and Industrial Aerodynamics, 2020, 196: 104046.

[25] WU Y C, CHEN X Z, WANG Y F. Identification of linear and nonlinear flutter derivatives of bridge decks by unscented Kalman filter approach from free vibration or stochastic buffeting response [J]. Journal of Wind Engineering and Industrial Aerodynamics, 2021, 214: 104650.

[26] LI W J, LAIMA S J, JIN X W, et al. A novel long short-term memory neural-network-based self-excited force model of limit cycle oscillations of nonlinear flutter for various aerodynamic configurations [J]. Nonlinear Dynamics, 2020, 100(3): 2071-2087.

[27] LI T, WU T, LIU Z. Nonlinear unsteady bridge aerodynamics: Reduced-order modeling based on deep LSTM networks [J]. Journal of Wind Engineering and Industrial Aerodynamics, 2020, 198: 104116.

[28] LIAO H L, MEI H Y, HU G, et al. Machine learning strategy for predicting flutter performance of streamlined box girders [J]. Journal of Wind Engineering and Industrial Aerodynamics, 2021, 209: 104493.

[29] MATSUMOTO M, DAITO Y, YOSHIZUMI F, et al. Torsional flutter of bluff bodies [J]. Journal of Wind Engineering and Industrial Aerodynamics, 1997, 69: 871-882.

[30] BHAT S S, GOVARDHAN R N. Stall flutter of NACA 0012 airfoil at low Reynolds numbers [J]. Journal of Fluids and Structures, 2013, 41: 166-174.

[31] HU C X, ZHAO L, GE Y J. A simplified vortex model for the mechanism of vortex-induced vibrations in a streamlined closed-box girder [J]. Wind and Structures, 2021, 32(4): 309-319.

[32] HU C X, ZHAO L, GE Y J. Multiple-order vertical vortex-induced vibration mechanism of a typical streamlined closed-box girder [J]. Journal of Wind Engineering and Industrial Aerodynamics, 2022, 227: 105066.

[33] BAIK Y S, BERNAL L P, GRANLUND K, et al. Unsteady force generation and vortex dynamics of pitching and plunging aerofoils [J]. Journal of Fluid Mechanics, 2012, 709: 37-68.

[34] PITT FORD C W, BABINSKY H. Lift and the leading-edge vortex [J]. Journal of Fluid Mechanics, 2013, 720: 280-313.

[35] ONOUE K, BREUER K S. Vortex formation and shedding from a cyber-physical pitching plate [J]. Journal of Fluid Mechanics, 2016, 793: 229-247.

[36] LI Z Y, FENG L H, KISSING J, et al. Experimental investigation on the leading-edge vortex formation and detachment mechanism of a pitching and plunging plate [J]. Journal of Fluid Mechanics, 2020, 901: A17.

[37] MIOTTO R, WOLF W, GAITONDE D, et al. Analysis of the onset and evolution of a dynamic stall vortex on a periodic plunging aerofoil [J]. Journal of Fluid Mechanics, 2022, 938: A24.

[38] STEVENS P R R J, BABINSKY H. Experiments to investigate lift production mechanisms on pitching flat plates [J]. Experiments in Fluids, 2016, 58(1): 7.

[39] MILLS R, SHERIDAN J, HOURIGAN K. Response of base suction and vortex shedding from rectangular prisms to transverse forcing [J]. Journal of Fluid Mechanics, 2002, 461: 25-49.

[40] Qin J X, Long J L, Zhang M J, et al. Long-range nighttime dynamic monitoring of long-span cable-stayed bridge with the enhanced bokeh tracking method using closing operation and Long Short-term Memory networks [J]. Engineering Structures, 2025, 342: 120913.

[41] Qin J X, Zhang M J, Long J L, et al. Bokeh-based target tracking for structural dynamic monitoring: A novel approach in variable lighting conditions [J]. Engineering Structures, 2024, 316: 118514.

[42] LUMLEY J L. The structure of inhomogeneous turbulent flows [M]// Atmospheric Turbulence and Radio Wave Propagation. Moscow: Nauka, 1967: 166-178.

[43] SCHMIDT O T, COLONIUS T. Guide to spectral proper orthogonal decomposition [J]. AIAA Journal, 2020, 58(3): 1023-1033.

[44] NEKKANTI A, SCHMIDT O T. Frequency-time analysis, low-rank reconstruction and denoising of turbulent

flows using SPOD [J]. Journal of Fluid Mechanics, 2021, 926: A26.

[45] WU J Z, LU X Y, ZHUANG L X. Integral force acting on a body due to local flow structures [J]. Journal of Fluid Mechanics, 2007, 576: 265-286.

[46] WU J Z, PAN Z L, LU X Y. Unsteady fluid-dynamic force solely in terms of control-surface integral [J]. Physics of Fluids, 2005, 17(9): 098102.

[47] DYNNIKOVA G Y, ANDRONOV P R. Expressions of force and moment exerted on a body in a viscous flow via the flux of vorticity generated on its surface [J]. European Journal of Mechanics-B/Fluids, 2018, 72: 293-300.

[48] HOWE M S. On the force and moment on a body in an incompressible fluid, with application to rigid bodies and bubbles at high and low Reynolds numbers [J]. Quarterly Journal of Mechanics & Applied Mathematics, 1995, 48 (3): 401-426.

8:1矩形平板颤振流固耦合机理试验研究

李文杰，赖马树金

（1.哈尔滨工业大学教育部结构动力行为与控制重点实验室,哈尔滨150090;2.哈尔滨工业大学土木工程智能防灾减灾工信部重点实验室,哈尔滨150090;3.哈尔滨工业大学土木工程学院,哈尔滨150090）

摘要：当前钝体平板颤振研究中,非定常流动与结构振动之间的相互作用机制尚未明晰。本文探究了8:1矩形平板颤振过程中前缘涡的形成与演化机制,为揭示颤振的流固耦合机理提供了新的视角。开展了一系列风洞试验,对8:1矩形平板的非线性颤振失稳特性进行了研究。采用粒子图像测速技术(PIV)和流场插值重构方法,获取了8:1矩形平板发生颤振前后完整的绕流场特征。为了进一步分析与颤振耦合频率相关的特征流态,将谱本征正交分解方法(SPOD)拓展至非惯性参考系,实现了非稳态振动边界下颤振绕流场重构和颤振相关特征流动结构提取,发现8:1矩形平板发生颤振时,前缘涡受结构振动诱导出现周期性拍动现象。对不同来流速度下拍动前缘涡结构进行相关性分析,结果表明,前缘涡演化随风速提高呈现出显著的相位前移现象,进而诱发气动力同样发生相位前移,最终导致颤振发生。

关键词：颤振;气动不稳定性;流固耦合;前缘涡;谱本征正交分解

中图分类号：U448.25